Analysis of the performance and stability of a passive recirculation loop for hydrogen delivery to a PEM fuel cell system

by

Erika Susanne Sutherland
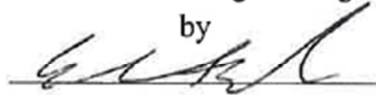
A Thesis

Submitted to the Faculty

of the

WORCESTER POLYTECHNIC INSTITUTE

In partial fulfillment of the requirements for the
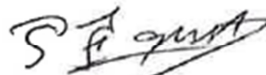Degree Master of Science
In
Mechanical Engineering
by

March, 2011
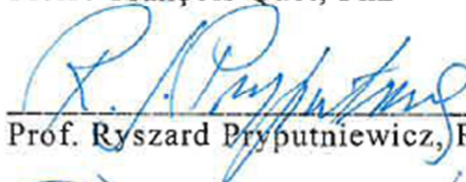
APPROVED:

WPI Faculty Advisor:

Prof. Mustapha. S. Fofana, PhD

Industry Mentor:

Pierre-François Quet, PhD

Committee Member:

Prof. Ryszard Pryputniewicz, PhD

Grand Committee Rep:

Prof. Richard Sisson, PhD

Abstract

Proton Exchange Membrane (PEM) fuel cells are becoming an increasingly important alternative to combustion engines as the fossil fuel reserves are depleted. Several papers have presented steady state analyses of the system, but few are known to present dynamic analysis of the flow and control of the hydrogen delivery process. This thesis presents the dynamic analysis of hydrogen delivery to a PEM fuel cell system. The hydrogen is delivered to the anode with use of an ejector for passive recirculation. The system to be studied consists of the manifolds, ejector, and pressure control valve. Models describing the elements of the anode delivery systems are formulated. The governing nonlinear equations are solved analytically and numerically, and the regimes of stable hydrogen delivery process are established. The linearized models are used for performance analysis and optimization of the hydrogen delivery process. The nonlinear model is used to improve the simulation of the dynamics of the PEM fuel cell system and validate the parameters at optimal linearized stability. Experiments are conducted to find the parameters used in the model, as well as validate the results. Both the linear and nonlinear models are implemented in Simulink and tested against the laboratory data from the PEM fuel cell system. The analysis showed that the models have the same time constant and dynamic behavior as the PEM system. The optimal parameters for stability and a faster response with no oscillations in the output are obtained. The redesigned valve and resulting dynamics of the PEM fuel cell system provides improved system performance.

i

Table of Contents

Nomenclature

VARIABLES		UNITS
k	linearized constant of restriction	(g/s)/Pa
K	spring constant	N/m
$\dot{m}$	mass flow rate	g/s
m	mass	kg
M	molar mass	g/mol
Mach	mach number	
p	pressure	Pa
$\dot{P}$	rate of change of the pressure	Pa/s
Rg	universal gas constant	(L atm)/mol K
R	radius	m
T	temperature	K
V	volume	L
v	velocity	m/s
ω	the ejector entrainment ratio	
Ψ	the coefficient of frictional losses in the ejector	
γ	specific heat ratio of the gas	

SUBSCRIPTS

im	inlet manifold
fc	fuel cell
om	outlet manifold
u	upstream
d	downstream
im,fc	between the inlet manifold and the fuel cell stack
fc,om	between the outlet manifold and the fuel cell stack
p	primary flow
r	recycle flow
s	supply

List of Figures

List of Tables

Acknowledgments

Chapter 1. Introduction to hydrogen fuel cells

Hydrogen fuel cell power has been increasingly studied over the last decade as the search for alternative energy sources has become more critical. There are two main factors driving the motivation for conversion to hydrogen power. The first is the imminent depletion of fossil fuel reserves and its direct impact on fuel prices. The second is the environmental concerns over increasing greenhouse gas (GHG) emissions. Studies have shown that an approximate 4% reduction in global emissions is possible with a transition of 80% of the vehicles on the road to hydrogen usage.[1] There is an expectation that this will occur by the year 2050.[1]   The leading technology for this transition is the proton exchange membrane (PEM) fuel cell. In order to demonstrate the capability of this technology, smaller fleet applications are being developed. These fleet applications include forklifts, buses, airport fleets, and city commuter transport.

The PEM fuel cell was originally invented by researchers at GE in the 1960s. The PEM fuel cell works by converting hydrogen and oxygen into water and electricity through a reaction that takes place inside the fuel cell stack. Hydrogen enters the stack on the anode side and air enters the stack on the cathode side. The catalyst in the proton exchange membrane between the anode and the cathode allows the hydrogen atom to free its electron and move from the anode to the cathode to bond with the oxygen and become water. The freed electron then becomes the electrical power the stack provides for its application.

The purpose of the following investigation is to model and improve the supply of hydrogen fuel to a PEM fuel cell stack in an automotive application. The proper

stoichiometric amounts of hydrogen and oxygen must be maintained within the stack to ensure that it can deliver the power required for its load. There are operating regimes in which some systems are occasionally unable to maintain enough hydrogen in the fuel cell during step changes in the stack current which causes an oscillation in the outlet pressure. The goal of this project is to find and eliminate these regimes by performing a stability analysis on the system and defining the range of parameters that will increase the system's performance and operating capacity. A nonlinear model is developed and then linearized for stability analysis. The modeling is focused on three main elements, the stack with inlet and outlet manifolds, the ejector which is used to recycle the excess hydrogen, and the pressure control valve which is used to control the pressure in the anode outlet manifold. The stability analysis of the system provides an opportunity to make modifications to the pressure control valve which improves the system's overall operation. The modification of this variable valve will allow a proper stoichiometry to be maintained within the stack throughout the systems operating regime.

The remainder of the report is characterized as follows. Chapter 2 provides a literature review of fuel cell system dynamic modeling and ejector system modeling. The model for the system is developed in Chapter 3. The necessary parameters for performance evaluation and stability analysis are found through experimentation and research. This parameter identification is presented in Chapter 4. The parameters are then used to evaluate the performance and stability of the PEM fuel cell system in Chapter 5 where the optimization of the parameters is also presented. The results of the model and its stability analysis are summarized in Chapter 6. The appendices contain the MATLAB code and programs that are developed for this study.

Chapter 2. Hydrogen fuel cell models and theory

2. Introduction

Proton exchange membrane fuel cells require consistent delivery of hydrogen and oxygen to the anode and cathode respectively in order to create an uninterrupted supply of electricity through the reactions

$$H_2 \rightarrow 2H^+ + 2e^-$$
(1)

on the anode side and

$$2H^+ + 2e^- + \frac{1}{2}O_2 \rightarrow H_2O$$
(2)
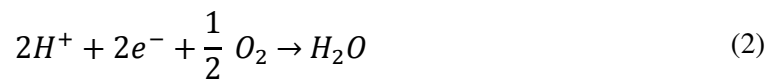
on the cathode side. These two reactions result in the overall reaction

$$H_2 + \frac{1}{2}O_2 \rightarrow H_2O$$
(3)

Most fuel cell systems use a blower or a compressor to provide air to the cathode of the stack. In order to sustain the reaction, the blower must provide enough air to the stack such that an oxygen stoichiometric ratio (stoich) of at least 1 is maintained. The anode side of the stack also requires a hydrogen stoich of at least 1 for the reaction, however a stoich greater than 1.25 is preferred to ensure that there is more than enough hydrogen available for the reaction[2]. At a hydrogen stoich of less than 1.25 the current distribution in the cell becomes heterogeneous and the fuel cell performance decreases [2]. The heterogeneous current distribution results in carbon corrosion and platinum dissolution [2]. Excess hydrogen is supplied to the anode side in order to avoid these phenomena. The unused hydrogen from the reaction is commonly recycled from the anode outlet of the stack back to its inlet through the use of an ejector. A common design for cathode and anode gas delivery is shown in Figure 1.
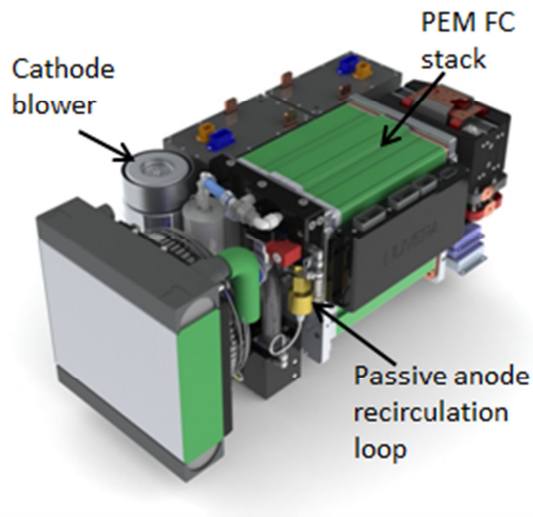
Figure 1: Standard Fuel Cell System

In the fuel cell, being studied in this thesis, the recycled hydrogen is also used to purge the anode of water which transferred from the cathode through the membrane and accumulated in the anode. This water accumulation can also cause localized fuel starvation and as a result cell reversal and carbon corrosion.[3] In order to achieve this water purging, a minimum pressure drop across the anode has to be maintained. This criterion requires a hydrogen stoich significantly greater than one to maintain a sufficient pressure drop. The fluid dynamics of the hydrogen flow through the inlet manifold, the stack and the outlet manifold is important to understand in order to ensure the proper pressure and flow are being delivered to the stack for the reaction. The performance of the ejector is also very important to the overall performance and stability of the system. The pressure control valve is responsible for controlling the flow of hydrogen to the ejector and the stack. Its behavior controls the performance and stability of the system. These three items will be modeled in detail and combined to analyze the system's response.

4

2.1 Existing stack and manifold models

Previous studies of similar systems have presented control models of the cathode air

and hydrogen gas. One such paper is written by Cheng et al. [4]. A dynamic model is

developed with a focus on control and stability analysis of the system, rather than the

steady-state requirements. The model also includes a humidifier prior to the anode, which

changes the dynamics of the system as compared with the fuel cell system studied here

which does not contain an anode humidifier; however, there are many similarities

between the system studied in the paper and the one analyzed here. This paper will thus

be used as a guideline for the model developed here. In particular, the transient response

of the inlet and outlet models can be directly applied. From the ideal gas law

$$PV = nRT, \qquad (4)$$

the dynamic of the pressure in a manifold can be found by differentiating (4) in time:

$$\frac{dP}{dt} = \frac{\dot{m}_{in} - \dot{m}_{out}}{M} \frac{R_g T}{V}, \qquad (5)$$

where M is the molecular weight of the gas, V is the volume of the manifold, P is the

pressure, T is the temperature, $\dot{m}_{in}$ is the mass flow rate of the gas entering the manifold

and $\dot{m}_{out}$ is the mass flow rate of the gas out of the manifold. This lumped volume

description will be used to model the dynamics of the anode volume in the stack and the

inlet and outlet manifolds.

Similar studies have been done by Jay T. Pukrushpan, Huei Peng, and Anna G.

Stefanopoulou [5], [6] . Their first paper presents a nonlinear model of a PEM fuel cell

system which is then linearized around 40kW[5]. The basic equations for mass balance are

presented in the paper for both the cathode and anode side flows. The paper however

does not address improvements which can be made to the control and the focus is on the system as whole rather than a direct focus on the hydrogen side delivery and control.

In the second paper a PEM fuel cell system model is presented for transient analysis.[6] In particular, the linearized nozzle flow equation which they present will be used in this model of a fuel cell system:

$$\dot{m} = k_{nozzel}(P_u - P_d) \tag{6}$$

where $\dot{m}$ is the mass flow rate of the gas through the restriction, k_{nozzel} is the linearized nozzle constant for the restriction, P_u is the upstream pressure and P_d is the downstream pressure. The model fully develops the pressures in the stack and manifolds subsystems, but does not include hydrogen recirculation through the use of an ejector, nor does it include the analysis of passive controller to deliver the proper hydrogen stoich and maintain pressure in the outlet manifold. The authors make the assumption that the stack temperature can be taken as constant during the analysis due to the time constant of the temperature response being much greater than the response time of the pressures in the system to a step change in stack current. The same assumption will be made in the stack model implemented here.

2.2 Existing ejector models

Ejectors work mainly as a result of the venturi effect [7]. High pressure gas comes into the ejector as the primary flow stream and is compressed through the throat of the ejector nozzle. As the gas expands after passing through the nozzle it creates suction causing the secondary flow to become entrained. The two flows then enter the constant area portion of the ejector where they mix and become a single stream at the exit of the ejector. Figure 2 provided by Huang et al.[8] shows the basic geometry of an ejector.
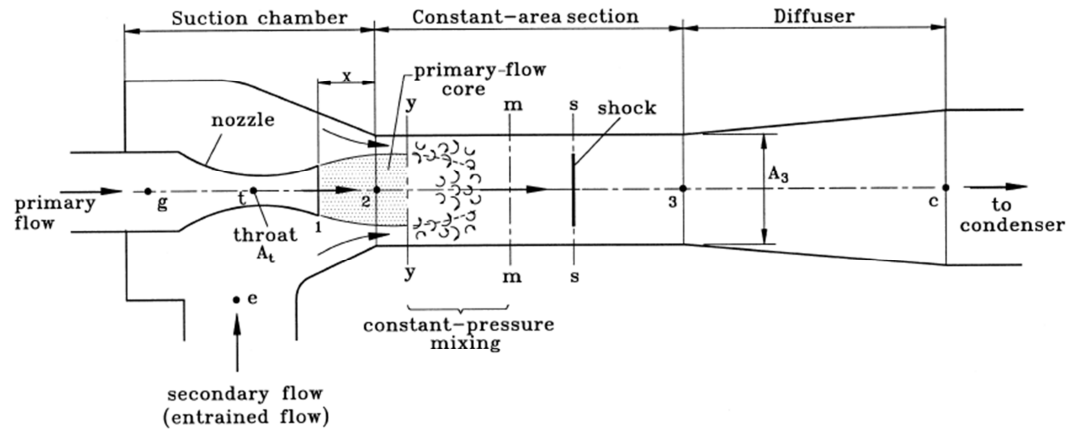
Figure 2: Basic Ejector Geometry

The ratio of the secondary mass flow rate over the primary mass flow rate is called the entrainment ratio of the ejector and is the main characteristic of an ejector.

A simplified ejector model for control and optimization has been presented by Yinhai Zhu et al[9]. In this paper they have compared the results of a more complex shock circle model to the simplified model they developed and found it to have equal or better accuracy. They have developed the entrainment ratio to be given by

7

$$\omega = b_1 f_1 \left(\frac{R_2}{R_t}\right)^2 \left(\frac{P_r}{P_p}\right) \left\{ 1 - b_2 \frac{R_t}{R_2} \left(\frac{P_p}{P_r}\right)^{\frac{\gamma+1}{4\gamma}} \left[\left(\frac{P_p}{P_r}\right)^{\frac{\gamma-1}{\gamma}} - 1 \right]^{-\frac{1}{4}} \right\} \tag{7}$$

where

$$b_1 = 2\psi_p^{-\frac{1}{2}} \left(\frac{1+\gamma}{2}\right)^{\frac{\gamma+1}{2(\gamma-1)}} \tag{8}$$

$$b_2 = \psi_{exp}^{-\frac{1}{2}} \left(\frac{\gamma-1}{2}\right)^{\frac{1}{4}} \left(\frac{\gamma+1}{2}\right)^{\frac{\gamma+1}{4(1-\gamma)}} \tag{9}$$

$$f_1 = \left(\frac{T_p}{T_{sA}}\right)^{\frac{1}{2}} \left[\frac{n}{n+1} - \frac{n}{2n+1}\left(1 - \frac{R_{pA}}{R_2}\right)\right], \tag{10}$$

ψ_p and ψ_{exp} are coefficients which account for the frictional losses during the mixing process in the suction chamber, R_t is the radius at the nozzle throat, R_2 is the radius after the nozzle in the constant area chamber prior to the diffuser and R_{pA} is the radius of the primary flow at the entrance to the constant area chamber, P_p is the pressure of the primary flow and P_r is the pressure of the secondary, or recycle flow, T_p is the temperature of the gas in the primary flow before entering the nozzle and T_{sA} is the temperature after it has passed through the nozzle and is entering the constant area chamber. The relationship between the ejector entrainment ratio and the pressure in the anode outlet can then be modeled using (6). This model is not implemented in this report as the results cannot be fitted to the data collected from the ejector used in the system.

A second paper, intended for modeling an ejector used to recycle gas to the anode of a solid oxide fuel cell (SOFC), is presented by Zhu et al[10]. In this paper a more

comprehensive model is developed for fuel recirculation in a fuel cell system. This model makes four assumptions. The first is that the diameter of the mixing chamber is much greater than the throat of the ejector. This assumption does apply to the PEM fuel cell ejector used on the system modeled in this study. The second assumption is that the primary and secondary flows are overheated gases rather than saturated vapors. The PEM fuel cell anode recirculation ejector in this study uses dry hydrogen as its primary flow, however the gas is at ambient temperature and the recycled flow contains saturated vapor. The third assumption is that the secondary flow temperature is very high. This third assumption does not apply here, because the secondary flow in the PEM fuel cell studied is approximately 80˚C. The fourth assumption does apply and is that the secondary pressure is much smaller than the primary pressure. Based on these assumptions the secondary mass flow rate is described as

$$\dot{m}_s = 2\pi\bar{\rho}v_{P,3}\left[\frac{n_v R_3{}^2}{n_v + 1}\right]\left(1 - \frac{R_{P,3}}{R_3}\right)^{\frac{n_v+1}{n_v}} - \frac{n_v R_3{}^2}{2n_v + 1}\left(1 - \frac{R_{P,3}}{R_3}\right)^{\frac{2n_v+1}{n_v}}, \qquad (11)$$

where $\bar{\rho}$ is the average density of the secondary flow. $v_{P,3}$ is the velocity of the primary flow at the entrance to the mixing chamber of the ejector, shown in the figure below obtained from Zhu et al[10].
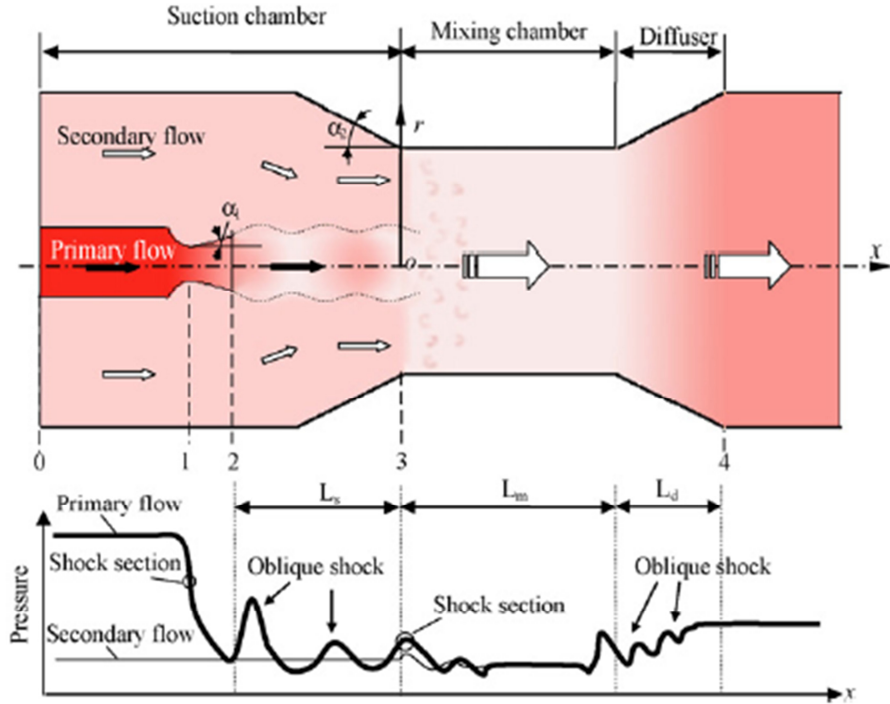
Figure 3: Ejector geometry from Zhu et al.[10]

Figure 3 shows the five critical geometry sections of the ejector. The radius of the mixing chamber R_3 and the radius of the primary flow at the inlet to the mixing chamber $R_{P,3}$ is shown in the figure at the section denoted by the number three. n_v is a function of $R_{P,3}$, R_3 and $Mach_{P,3}$ where $Mach_{P,3}$ is the Mach number of the primary flow at the inlet to the mixing chamber. n_v is expressed as

$$n_v = \frac{ln\left(1 - \frac{R_{P,3}}{R_3}\right)}{-ln(Mach_{P,3})}. \tag{12}$$

$Mach_{P,3}$ can be calculated using energy balance, which results in the following equation

$$Mach_{P,3} = \sqrt{\frac{2\left(\frac{P_{P,0}}{P_{S,0}}\right)^{\frac{\gamma-1}{\gamma}} - 2}{\gamma - 1}} \qquad (13)$$

where $P_{P,0}$ and $P_{S,0}$ are the pressures of the primary and secondary flows at the entrance to the ejector suction chamber and γ is the specific heat ratio of the gas. $V_{P,3}$ can then be found from the mach number using

$$V_{P,3} = Mach_{P,3}\sqrt{\gamma R_g T_{S,0}} \qquad (14)$$

where R_g is the universal gas constant and $T_{S,0}$ is the temperature of the secondary flow at the inlet to the suction chamber. Finally, $R_{P,3}$ can be found through mass and energy balance equations to determine the expansion of the gas after passing through the throat, and is given by

$$R_{P,3} = \frac{D_t}{2\zeta_{exp}}\sqrt{\frac{1}{Mach_{P,3}}}\left(\frac{2 + (\gamma - 1)Mach_{P,3}^{\,2}}{\gamma + 1}\right)^{\frac{\gamma+1}{4(\gamma-1)}} \qquad (15)$$

where D_t is the throat diameter of the ejector and ζ_{exp} is a coefficient that accounts for the frictional losses due to the mixing of the two flows.

A third paper by Huang et al. [8] presents a1-D analysis of ejector performance. This paper also makes several assumptions in order to create a working model in one dimension. The analysis assumes that the working fluid is an ideal gas with constant thermodynamic properties. It also assumes that the flow in the ejector is stead and one dimensional and that the kinetic energy at the inlets of the primary and suction ports and

11

the exit of the diffuser is negligible. The inner wall of the ejector is considered to be adiabatic and the frictional losses in the ejector due to mixing are accounted for through the use of a coefficient which can be found through testing. In this model the entrained flow is

$$\dot{m}_s = \sqrt{\zeta_s}\frac{P_s A_{sy}}{\sqrt{T_s}}\sqrt{\frac{\gamma}{R}\left(\frac{2}{\gamma+1}\right)^{\frac{\gamma+1}{\gamma-1}}} \tag{16}$$

where ζ_s is a coefficient that is related to the isentropic efficiency of the entrained flow and A_{sy} is the area of the secondary flow at section y-y as shown in figure 2 obtained from Huang et al[8].

After the testing and development of each of these models against the ejector data taken later in the report, the second model from Zhu et al.[9] was implemented using a choked flow equation for the primary flow through the ejector orifice, however it was unused because the coefficient ζ_s, needed to be adjusted for different back pressures. The choked flow equation was chosen because the orifice in the ejector used in the system studied does not have a diffusing geometry after the throat but rather is designed as a flat plate orifice. The equation works well, once fitted to a constant back pressure condition, however since the back pressure is not constant in the system a curve from a data fit is implemented in the nonlinear model.

Chapter 3. Model development

3. Introduction

The PEM fuel cell stack's power output is dependent on the stable delivery of fuel to its anode. The goal of the system to be analyzed is to deliver hydrogen at a rate equal to the rate at which it is being consumed by the stack to produce current. This controlled flow rate is achieved in the system by maintaining the outlet manifold pressure, P_{om}, at a constant pressure. For performance, however, the stack requires a flow through the anode greater than the flow rate at which hydrogen is being consumed, therefore a recirculation loop with an ejector is used to recirculate hydrogen from the anode outlet back into the stack. This passive recirculation loop increases the flow rate through the stack in order to purge water out of the stack as well as maintain a hydrogen stoich greater than 1.25. The recirculation loop is regularly purged to remove the water and nitrogen that crosses over from the cathode and accumulates in the anode during operation.

The system can be described as follows. A hydrogen inlet valve opens allowing hydrogen at the supply pressure, P_s which is approximately 200 psig, to enter into a mechanical pressure control valve that is designed to maintain the anode outlet pressure, P_{om}, to be between 7-9 psig. The valve controls the flow by changing the distance of the plunger from valve seat. The orifice moves in x by the displacement of the piston on the valve. The displacement of the piston is controlled through a spring which prevents the valve from closing until the force created by the pressure in the outlet manifold times the area of the valve piston exceeds the force of the spring. This is shown schematically in Figure 4.

The hydrogen leaves the control valve and then enters the ejector where it mixes with the recycled hydrogen, nitrogen, and water vapor. It then enters the anode side of the stack, which can be modeled as a variable bleed restriction based on the fuel cell current. The remaining hydrogen, mixed with the nitrogen and water vapor, then exits the stack and enters the anode outlet manifold where it is recycled by the ejector until purged.

The pressure from the tanks and regulator through the inlet valve will be considered constant for the purpose of the system stability analysis. The pressure does changes slowly over a four hour period as the tanks are emptied but can be considered constant when looking at the system operation since all of the system dynamics of interest are on time scales of a few seconds or less. Therefore the schematic of the system to be analyzed with mass flow rates in and out of the components can be represented as shown in Figure 4. The dynamics of the system will be modeled in two sections, the fuel cell plant and the pressure control valve. The two models will then be combined for simulation and stability and performance analysis.
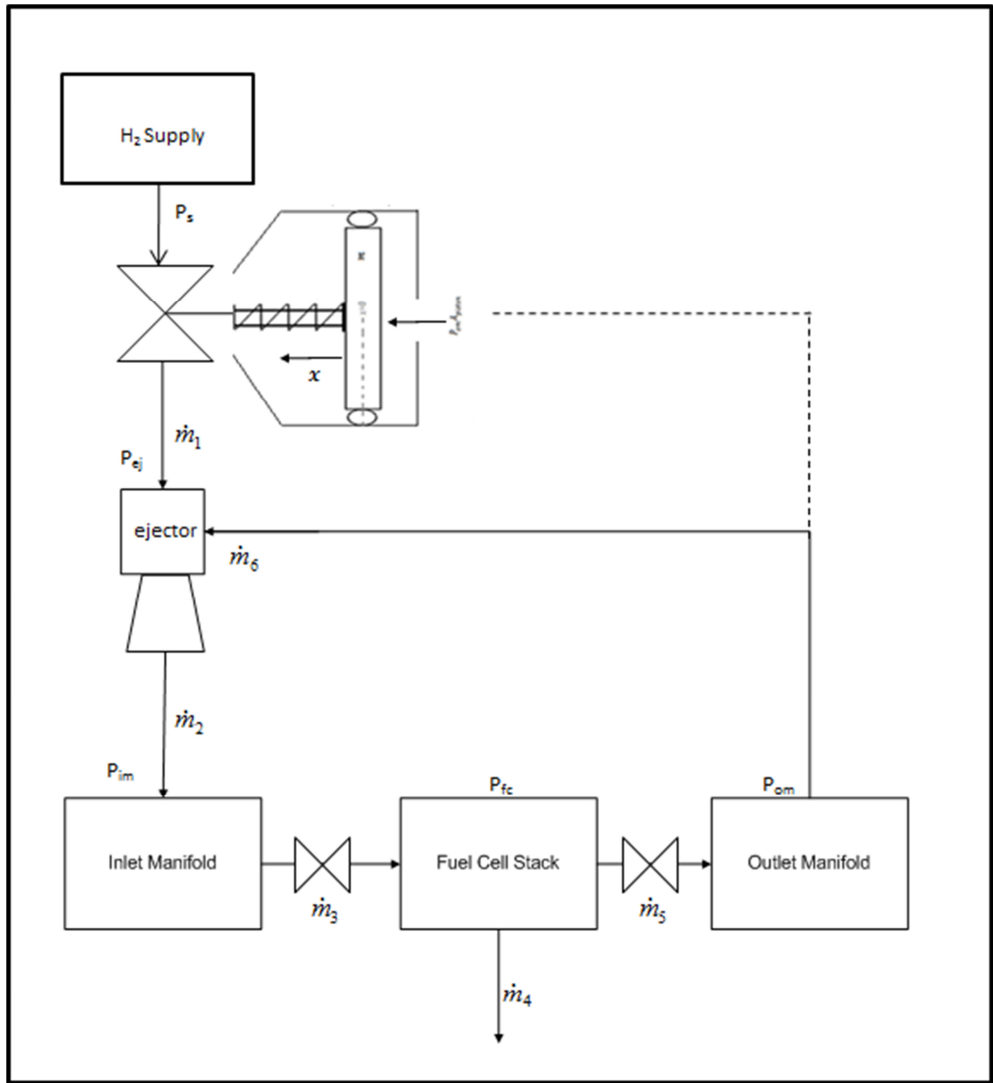
Figure 4: System control schematic

3.1 Fuel cell plant model formulation

The model makes several assumptions for simplification. These assumptions include modeling the stack as a single volume and ignoring water accumulation in the stack. It also assumes that the temperature in the stack is constant. This is a good approximation while the system is in its continuous operating mode, but is not valid at start up. The model assumes that the hydrogen coming into the system from the tanks is at 23°C. Additionally, the assumption is made that due to the regular purge routine the gas composition does not change significantly during operation. The dynamics during the times when the system is purging the anode loop of nitrogen are not considered in this model.

The mass flow rate $\dot{m}_6$ that is recycled through the ejector is equal to the entrainment ratio ω of the ejector times the motive flow into the ejector $\dot{m}_1$. For stability analysis ω will be considered constant, which will be justified in Chapter 4. In the system model the ejector entrainment ratio will be calculated as a function of the inlet pressure P_{ej} and the pressure of the recycle flow P_{om}, with a relationship that will be determined from test data. The recycled flow from the outlet manifold is

$$\dot{m}_6 = \omega \dot{m}_1,$$
(17)

and the flow out of the ejector $\dot{m}_2$ is

$$\dot{m}_2 = \dot{m}_1 + \dot{m}_6.$$
(18)

The mass flow rate from the inlet manifold into the stack $\dot{m}_3$ is given by the following equation which relates the difference in the pressure in the inlet manifold P_{im} and the pressure in the fuel cell P_{fc} to the flow rate into the stack

$$\dot{m}_3 = k_{im,fc}(P_{im} - P_{fc}), \tag{19}$$

where $k_{im,fc}$ is the linearized nozzle constant. A similar equation is used to relate the mass flow rate $\dot{m}_5$ to the difference in the pressure in the stack P_{fc} to the pressure in the outlet manifold P_{om}, namely

$$\dot{m}_5 = k_{fc,om}(P_{fc} - P_{om}), \tag{20}$$

where $k_{fc,om}$ is linearized nozzle constant.

The rate of change of the pressure in the inlet manifold, stack and outlet manifolds, $\dot{P}_{im}$, $\dot{P}_{fc}$, and $\dot{P}_{om}$ respectively, can then be developed from the ideal gas law as was presented in (5):

$$\dot{P}_{im} = \frac{R_g T}{M_{im} V_{im}} (\dot{m}_2 - \dot{m}_3) \tag{21}$$

$$\dot{P}_{fc} = \frac{R_g T}{M_{fc} V_{fc}} (\dot{m}_3 - \dot{m}_4 - \dot{m}_5) \tag{22}$$

$$\dot{P}_{om} = \frac{R_g T}{M_{om} V_{om}} (\dot{m}_5 - \dot{m}_6) \tag{23}$$

where R_g is the universal gas constant, T is the gas temperature, M is the molar mass of the gas, and V is the volume of the chamber. $\dot{m}_4$ in (22) is the mass flow rate of the hydrogen that is being consumed by the stack to produce current. Then defining

17

$$k_{im} = \frac{R_g T}{M_{im} V_{im}} \tag{24}$$

$$k_{fc} = \frac{R_g T}{M_{fc} V_{fc}} \tag{25}$$

$$k_{om} = \frac{R_g T}{M_{om} V_{om}} \tag{26}$$

(21), (22) and (23) become

$$\dot{P}_{im} = k_{im}(\dot{m}_2 - \dot{m}_3) \tag{27}$$

$$\dot{P}_{fc} = k_{fc}(\dot{m}_3 - \dot{m}_4 - \dot{m}_5) \tag{28}$$

$$\dot{P}_{om} = k_{om}(\dot{m}_5 - \dot{m}_6). \tag{29}$$

Since $\dot{m}_1$ and $\dot{m}_4$ are both exogenous variables to the anode model the rate of change of the system pressures can be rewritten as

$$\dot{P}_{im} = k_{im}\left(\dot{m}_1 + \omega \dot{m}_1 - k_{im,fc}(P_{im} - P_{fc})\right) \tag{30}$$

$$\dot{P}_{fc} = k_{fc}\left(k_{im,fc}(P_{im} - P_{fc}) - \dot{m}_4 - k_{fc,om}(P_{fc} - P_{om})\right) \tag{31}$$

$$\dot{P}_{om} = k_{om}\left(k_{fc,om}(P_{fc} - P_{om}) - \omega \dot{m}_1\right), \tag{32}$$

which can then be expanded and written in the state space format as

$$\dot{P} = AP + Bu \tag{33}$$

where

$$P = \begin{bmatrix} P_{im} \\ P_{fc} \\ P_{om} \end{bmatrix}, \quad u = \begin{bmatrix} \dot{m}_1 \\ \dot{m}_4 \end{bmatrix}, \tag{34}$$

$$A = \begin{bmatrix} -k_{im}k_{im,fc} & k_{im}k_{im,fc} & 0 \\ k_{fc}k_{im,fc} & -k_{fc}(k_{im,fc} + k_{fc,om}) & k_{fc}k_{fc,om} \\ 0 & k_{om}k_{fc,om} & -k_{om}k_{fc,om} \end{bmatrix} \quad (35)$$

and

$$B = \begin{bmatrix} k_{im}(1 + \omega) & 0 \\ 0 & -k_{fc} \\ -k_{om}\omega & 0 \end{bmatrix}. \quad (36)$$

Equation (33) is used to describe the fuel cell plant dynamics and is implemented both

the linear and nonlinear models of the closed loop system.

3.2 Steady state evaluation of the fuel cell plant

Equations (30) through (32) can be used to prove that by controlling P_{om} to a constant value the flow into the system $\dot{m}_1$ is maintained at an equal to the mass flow rate of the hydrogen consumed by the stack $\dot{m}_4$. At steady state, where $\dot{P}_{im} = \dot{P}_{fc} = \dot{P}_{om} = 0$, solving equations(30) through (32) for this condition yields:

$$0 = k_{im}\left(\dot{m}_1 + \omega\dot{m}_1 - k_{im,fc}(P_{im} - P_{fc})\right) \tag{37}$$

$$0 = k_{fc}\left(k_{im,fc}(P_{im} - P_{fc}) - \dot{m}_4 - k_{fc,om}(P_{fc} - P_{om})\right) \tag{38}$$

$$0 = k_{om}\left(k_{fc,om}(P_{fc} - P_{om}) - \omega\dot{m}_1\right). \tag{39}$$

Dividing (37) by k_{im}, and (38) by k_{fc} and (39) by k_{om} results in:

$$0 = \dot{m}_1 + \omega\dot{m}_1 - k_{im,fc}(P_{im} - P_{fc}) \tag{40}$$

$$0 = k_{im,fc}(P_{im} - P_{fc}) - \dot{m}_4 - k_{fc,om}(P_{fc} - P_{om}) \tag{41}$$

$$0 = k_{fc,om}(P_{fc} - P_{om}) - \omega\dot{m}_1. \tag{42}$$

Combining (41) and (42) then gives

$$0 = k_{im,fc}P_{im} - k_{im,fc}P_{fc} - \dot{m}_4 - \omega\dot{m}_1, \tag{43}$$

and combining (43) and (40) results in

$$0 = \dot{m}_1 + \omega\dot{m}_1 - \dot{m}_1 - \omega\dot{m}_1 = \dot{m}_1 - \dot{m}_4, \tag{44}$$

which simplifies to

$$\dot{m}_1 = \dot{m}_4. \tag{45}$$

This shows that for the system to reach a steady state condition where $\dot{P}_{im} = \dot{P}_{fc} = \dot{P}_{om} = 0$, the flow rate of the hydrogen to the stack must be equal to the amount consumed by the stack.

3.3 Stability analysis of the fuel cell plant

The stability of the system without the control valve in place and assuming a constant ejector entrainment ratio is found from studying the stability of (33). The system's stability can be analyzed by examining the eigenvalues of system state matrix A[11].

The eigenvalues are found by solving for the values of λ in

$$|\lambda I - A| = 0, \tag{46}$$

where I is the identity matrix and λ can be any number real or complex. This is equivalent to

$$\begin{vmatrix} \lambda + k_{im}k_{im,fc} & -k_{im}k_{im,fc} & 0 \\ -k_{fc}k_{im,fc} & \lambda + k_{fc}(k_{im,fc} + k_{fc,om}) & -k_{fc}k_{fc,om} \\ 0 & -k_{om}k_{fc,om} & \lambda + k_{om}k_{fc,om} \end{vmatrix} = 0, \tag{47}$$

which becomes

$$\begin{aligned}(\lambda + k_{im}k_{im,fc})&\{(\lambda + k_{fc}(k_{im,fc} + k_{fc,om}))(\lambda + k_{om}k_{fc,om}) \\ &- (-k_{om}k_{fc,om})(-k_{fc}k_{fc,om})\} \\ &- (-k_{im}k_{im,fc})\{(-k_{fc}k_{im,fc})(\lambda + k_{om}k_{fc,om})\} = 0. \end{aligned}\tag{48}$$

(48) can then be expanded and simplified as

$$\begin{aligned}\lambda\big[\lambda^2 &+ \lambda(k_{fc}k_{im,fc} + k_{fc}k_{fc,om} + k_{im}k_{im,fc} + k_{om}k_{fc,om}) \\ &+ (k_{fc}k_{im}k_{im,fc}k_{fc,om} + k_{fc}k_{om}k_{im,fc}k_{fc,om} \\ &+ k_{im}k_{om}k_{im,fc}k_{fc,om})\big] = 0. \end{aligned}\tag{49}$$

By letting

$$\alpha_1 = (k_{fc}k_{im}k_{im,fc}k_{fc,om} + k_{fc}k_{om}k_{im,fc}k_{fc,om} + k_{im}k_{om}k_{im,fc}k_{fc,om}) \tag{50}$$

22

and

$$\alpha_2 = (k_{fc}k_{im,fc} + k_{fc}k_{fc,om} + k_{im}k_{im,fc} + k_{om}k_{fc,om}),\qquad(51)$$

Equation (49) can be written as

$$\lambda[\lambda^2 + \alpha_2\lambda + \alpha_1] = 0.\qquad(52)$$

Since α_1 and α_2 are real and positive, the roots of $\lambda^2 + \alpha_2\lambda + \alpha_1$ are real and negative

and therefore the solutions of (52) are

$$\lambda_1 = 0,\qquad(53)$$

$$\lambda_2 = -\alpha_2 + \frac{\sqrt{\alpha_2{}^2 - 4\alpha_1}}{2},\qquad(54)$$

$$\lambda_3 = -\alpha_2 - \frac{\sqrt{\alpha_2{}^2 - 4\alpha_1}}{2}.\qquad(55)$$

Thus the fuel cell plant dynamics consist of one integrator and two stable modes. The physical understanding of the integrator can be had by returning to Figure 4 and recognizing that the fuel cell system has a fixed volume with one mass flow rate in $\dot{m}_1$, and one mass flow rate out $\dot{m}_4$. Due to this, the mass contained within the volume at any given time is equal to the integral of the flow entering it minus the flow leaving it.

3.4 Pressure control valve model formulation

The pressure control valve (PCV) is used to control the outlet manifold to a constant pressure, $\dot{P}_{om} = 0$. Implementation of a successful controller ensures that the mass flow rate $\dot{m}_1$ into the stack is equal to $\dot{m}_4$ on average, with in the response time of the controller. This prevents the stack from becoming starved for fuel and prevents over pressure conditions. The valve controls the flow of $\dot{m}_1$ through the use of a plunger that can move closer and further from the valve orifice to restrict or open the flow. This relationship allows the PCV to be modeled as a variable flow restriction for which the linearized flow constant of the valve k_{pcv} is given by a function of the displacement of the piston x

$$\dot{m}_1 = k_{pcv}(x)\left(P_s - P_{ej}\right), \tag{56}$$

where P_s is the supply pressure to the inlet of the valve and P_{ej} is the pressure at the inlet to the ejector. The schematic of the piston inside the valve body is given in Figure 5. The area of the plunger which makes contact with the orifice to fully close the valve is called the seat. The plunger is moved by a piston that is referenced to P_{om}, the pressure in the outlet manifold on one side and ambient pressure on the other side. The piston has an O-ring around the outside of it to seal the hydrogen from leaking past the piston. This O-ring is lubricated with a grease to allow for lower friction as the piston moves back and forth based on the reference pressure. The pressure force on the piston is balanced by a spring which it is compressed as the piston moves forward in x, as well as the pressure of the supply gas plunger seat which contacts the piston. The initial compression of the

24

spring, x_{offset} sets the pressure at which the valve begins to close. Figure 5 shows the free body diagram of the dynamics described here.
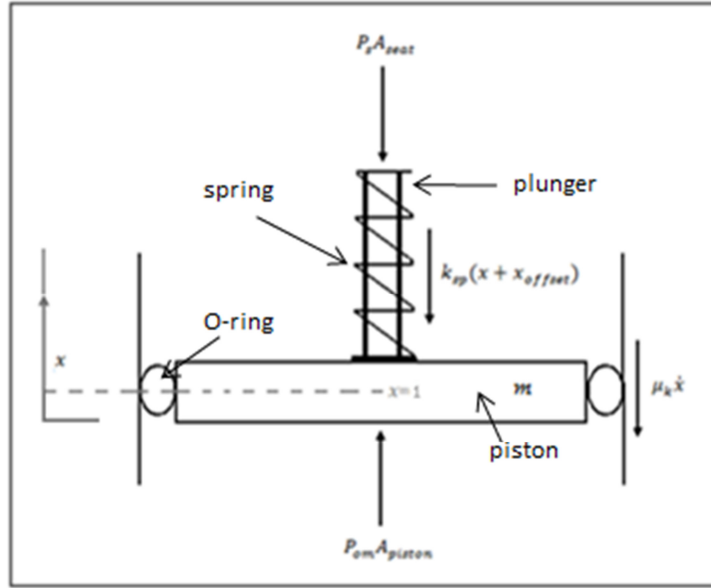
Figure 5: Free body diagram of the PCV piston

Newton's second law of motion applied to the PCV's piston results in

$$m\ddot{x} = -K_{sp}\left(x + x_{offset}\right) - P_s A_{seat} - \mu_k \dot{x} + P_{om}A_{piston}, \tag{57}$$

where m is the mass of the piston, K_{sp} is the spring constant, x_{offset} is the intial compression of the spring when the valve is assembled, P_s is the supply pressure, A_{seat} is the area of the plunger seat and A_{piston} is the area of the valve piston. In this equation the friction is a function of the velocity of the piston and is given as $\mu_k \dot{x}$ this modeled after the sliding friction relationships given in the Modern Tribology Handbook for a lubricated interface [12]. k_{pcv} can be related to the displacement x of the piston by

$$k_{pcv}(x) = k_{max} - \frac{k_{max}}{x_{max}} x,$$

(58)

where k_{max} is the maximum linearized nozzle constant for the valve and x_{max} is the

maximum displacement of the piston in the valve. Combining (56) and (58) yields

$$\dot{m}_1 = \left(k_{max} - \frac{k_{max}}{x_{max}} x \right) (P_s - P_{ej}).$$

(59)

As will be shown in Chapter 4, from lab testing we have the following relationship

between P_{ej} and $\dot{m}_1$:

$$\dot{m}_1 = k_{ej} P_{ej}.$$

(60)

Where k_{ej} is the linearized flow constant of the ejector. From (59) and (60)

$$x = x_{max} - \alpha \left(\frac{\dot{m}_1}{\beta - \dot{m}_1} \right),$$

(61)

where $\alpha = \frac{x_{max} k_{ej}}{k_{max}}$ and $\beta = P_s k_{ej}$.

Thus the nonlinear dynamics of the valve are fully represented by (57) and (61). These

two equations will be implemented in the nonlinear simulation of the valve.

3.5 Steady state evaluation of P_{om}

The steady state value of P_{om} is important because it is preferable to maintain the anode loop at pressure similar to the pressure of the cathode side because the cross-over of gasses through the membrane is proportional to the partial pressure differential between the anode and the cathode.. The steady state value of P_{om} can be found by evaluating (57) at $\dot{x} = \ddot{x} = 0$, which results in

$$P_{om} = \frac{K_{sp}(x + x_{offset}) + P_s A_{seat}}{A_{piston}}. \tag{62}$$

From (62) the maximum and minimum controlled steady state values of P_{om}, which are respectively P_{om_max} and P_{om_min}, can be found by letting $x = x_{max}$ and $x = 0$ which results in:

$$P_{om\_max} = \frac{K_{sp}(x_{max} + x_{offset}) + P_s A_{seat}}{A_{piston}}, \tag{63}$$

and

$$P_{om\_min} = \frac{K_{sp}(x_{offset}) + P_s A_{seat}}{A_{piston}}. \tag{64}$$

3.6 Linearization of the controller model

For the purpose of stability analysis of the system it is convenient to linearize the PCV dynamics around the midpoint of the range of $\dot{m}_1$. From equations (59) and (60) the maximum value of $\dot{m}_1$ occurs at $x = 0$, and is

$$\dot{m}_{1\_max} = \frac{k_{max} P_s k_{ej}}{k_{max} + k_{ej}}. \tag{65}$$

Also from (59) and (60), the minimum value of $\dot{m}_1$ occurs at $x = x_{max}$, and is equal to zero. There for the midpoint of the range of $\dot{m}_1$ is

$$l = \dot{m}_{1\_max}/2. \tag{66}$$

Then the Taylor series expansion of (61) around the midpoint of the range of $\dot{m}_1$ is

$$x = x_{max} - \frac{\alpha l}{\beta - l} - \frac{\alpha \beta}{(\beta - l)^2}(\dot{m}_1 - l) + H.O.T.. \tag{67}$$

Ignoring the higher order terms (H.O.T.) this can be expanded as

$$x = x_{max} - \frac{\alpha l}{\beta - l} + \frac{\alpha \beta l}{(\beta - l)^2} - \frac{\alpha \beta \dot{m}_1}{(\beta - l)^2}. \tag{68}$$

Defining

$$\delta = x_{max} - \frac{\alpha l}{\beta - l} + \frac{\alpha \beta l}{(\beta - l)^2} \tag{69}$$

and

$$\gamma = -\frac{\alpha\beta}{(\beta - l)^2}, \tag{70}$$

the linearized relationship between x and $\dot{m}_1$ is

$$x = \gamma\dot{m}_1 + \delta. \tag{71}$$

From (71) we also have the relationships

$$\dot{x} = \gamma\ddot{m}_1 \tag{72}$$

$$\ddot{x} = \gamma\dddot{m}_1. \tag{73}$$

Thus the linearized dynamics of the PCV can be represented by substituting (71) through (73) into (57) to obtain

$$m\gamma\dddot{m}_1 + \mu_k\gamma\ddot{m}_1 + k_{sp}\gamma\dot{m}_1$$

$$= -P_s A_{seat} + P_{om} A_{piston} - k_{sp}\delta - K_{sp} x_{offset}. \tag{74}$$

The linear dynamics of the PCV can be represented in state space as

$$\begin{bmatrix} \dot{z}_1 \\ \dot{z}_2 \end{bmatrix} = \begin{bmatrix} 0 & 1 \\ -\dfrac{K_{sp}}{m} & -\dfrac{\mu_k}{m} \end{bmatrix} \begin{bmatrix} z_1 \\ z_2 \end{bmatrix} + \begin{bmatrix} 0 \\ \dfrac{A_{piston}}{m\gamma} \end{bmatrix} P_{om} \tag{75}$$

and

$$\dot{m}_1 = \begin{bmatrix} 1 & 0 \end{bmatrix} \begin{bmatrix} z_1 \\ z_2 \end{bmatrix} - \frac{d}{k_{sp}\gamma}, \tag{76}$$

where

$$d = -P_s A_{seat} - k_{sp}\delta - K_{sp}x_{offset} \tag{77}$$

$$z_1 = \dot{m}_1 + \frac{d}{k_{sp}\gamma}, \quad \text{and} \quad z_2 = \dot{z}_1. \tag{78}$$

Equations (75) and (76) will be used in the linear model of the valve. This equation will

be combined with the linear plant equation, (33), in order study the valve's stability and

to obtain a single linear state space model for the closed system.

3.7 Stability of the controller

The stability of the controller can be analyzed by looking at the eigenvalues of the state matrix of the linearized system. The eigenvalues are found by

$$det \begin{pmatrix} 0 - \lambda & 1 \\ -\dfrac{K_{sp}}{m} & -\dfrac{\mu_k}{m} - \lambda \end{pmatrix} = 0 , \tag{79}$$

which is equivalently

$$\lambda^2 + \frac{\mu_k}{m} \lambda + \frac{K_{sp}}{m} = 0. \tag{80}$$

$\frac{\mu_k}{m}$ and $\frac{K_{sp}}{m}$ are both positive so the eigenvalues that result from the solution of the roots of (80), are both real and negative. They are

$$\lambda_1 = -\frac{\mu_k}{m} + \sqrt{\frac{\left(\frac{\mu_k}{m}\right)^2 - 4\frac{K_{sp}}{m}}{2}} \tag{81}$$

and

$$\lambda_2 = -\frac{\mu_k}{m} - \sqrt{\frac{\left(\frac{\mu_k}{m}\right)^2 - 4\frac{K_{sp}}{m}}{2}} . \tag{82}$$

Since λ_1 and λ_2 are both real and negative the PCV is always stable.

31

3.8 Closed loop system model and stability

To determine the stability of the system as a whole, the combined equation for the controller (the PCV) and the plant (the fuel cell and manifolds) is examined. From (33) we have

$$
\begin{bmatrix} \dot{P}_{im} \\ \dot{P}_{fc} \\ \dot{P}_{om} \end{bmatrix} = \begin{bmatrix} -k_{im}k_{im,fc} & k_{im}k_{im,fc} & 0 \\ k_{fc}k_{im,fc} & -k_{fc}(k_{im,fc}+k_{fc,om}) & k_{fc}k_{fc,om} \\ 0 & k_{om}k_{fc,om} & -k_{om}k_{fc,om} \end{bmatrix} \begin{bmatrix} P_{im} \\ P_{fc} \\ P_{om} \end{bmatrix}
$$
$$
+ \begin{bmatrix} k_{im}(1+\omega) \\ 0 \\ -k_{om}\omega \end{bmatrix} \dot{m}_1 + \begin{bmatrix} 0 \\ -k_{fc} \\ 0 \end{bmatrix} \dot{m}_4.
$$

(83)

Combining this with the linear representation of the valve (77) and (78), (83) can be rewritten as

$$
\begin{bmatrix} \dot{P}_{im} \\ \dot{P}_{fc} \\ \dot{P}_{om} \\ \dot{z}_1 \\ z_2 \end{bmatrix}
$$

$$
= \begin{bmatrix} -k_{im}k_{im,fc} & k_{im}k_{im,fc} & 0 & k_{im}(1+\omega) & 0 \\ k_{fc}k_{im,fc} & -k_{fc}(k_{im,fc}+k_{fc,om}) & k_{fc}k_{fc,om} & 0 & 0 \\ 0 & k_{om}k_{fc,om} & -k_{om}k_{fc,om} & -k_{om}\omega & 0 \\ 0 & 0 & 0 & 0 & 1 \\ 0 & 0 & \dfrac{A_{piston}}{m\gamma} & -\dfrac{\mu_k}{m} & -\dfrac{K_{sp}}{m} \end{bmatrix} \begin{bmatrix} P_{im} \\ P_{fc} \\ P_{om} \\ z_1 \\ z_2 \end{bmatrix}
$$

(84)

$$
+ \begin{bmatrix} 0 \\ -k_{fc} \\ 0 \\ 0 \\ 0 \end{bmatrix} \dot{m}_4 + \begin{bmatrix} -k_{im}(1+\omega) \\ 0 \\ k_{om}\omega \\ 0 \\ 0 \end{bmatrix} \frac{d}{k_{sp}\gamma}.
$$

This equation represents the complete linearized dynamics of the fuel cell and the valve. The closed loop system stability can then be analyzed by evaluating the eigenvalues of

32

the state matrix, which will be referred to as H in the remainder of the report. Since there is not a closed form solution to a fifth order polynomial, the stability will be evaluated numerically in section 5.4.

The nonlinear model of the closed system will be implemented using the linear plant model and the nonlinear valve model given by (57) and (61). The ejector entrainment ratio used in the simulation will be produced from a curve fit of the ejector test data given in Chapter 4.

Chapter 4. Parameter identification

4. Introduction

The next step is to develop the quantitative model by assigning values to the constants in the equations above. This requires a careful study of the fuel cell system and components. The component parameters are identified through analysis of the component drawings and through experimental results. The stack and stack manifold drawings were carefully studied to calculate the total volume for the stack and each manifold. The tubing lengths in the recirculation loop and interior volumes of the components are accounted for. A full characterization test is performed on the ejector to obtain its primary flow rate and entrainment ratio as a function of inlet pressure and back pressure. The pressure control valve is disassembled, measured and tested for the various parameters relevant to the model.

4.1 Identification of stack model parameters

The stack parameters k_{im}, k_{fc}, and k_{om} will be calculated for a $\dot{m}_1$ composition of 70% hydrogen and 30% nitrogen at room temperature in the model. The volumes have been calculated using the drawings of the system and previous knowledge of the stack performance. Using (5) with $M_{im} = M_{fc} = M_{om} = 9.82\ g/mol$, $V_{im} = 0.232L$, $V_{fc} = 6.32L$ and $V_{om} = 0.60L$, the values of k_{im}, k_{fc}, and k_{om} are accordingly

$$k_{im} = 1.093 * 10^6 \frac{Pa}{g}$$

$$k_{fc} = 4.0191 * 10^4 \frac{Pa}{g}$$

$$k_{om} = 4.233 * 10^5 \frac{Pa}{g}.$$

The values for $k_{im,fc}$ and $k_{fc,om}$ were found through testing of the stack's subsystem and knowledge of the pressure drop through the cells of the stack. Previous testing and CFD analysis performed by the stack manufacturer shows that the pressure drop through the stack cell accounts for approximately 30% of the pressure drop from the inlet manifold to the outlet manifold. The remaining 70% of the pressure drop is distributed between the inlet and outlet stack gasket. In this model however, the stack pressure drop is included in $k_{im,fc}$ and $k_{fc,om}$.

In order to obtain the flow versus pressure drop curve for the stack the system was tested at several different currents and the pressure into the ejector P_{ej}, the inlet manifold pressure P_{im} and the outlet manifold pressure P_{om} was recorded. The flow through the stack $\dot{m}_2$ was calculated by taking P_{ej} at each current from Figure 6 and by using Figure 11, in the ejector characterization section, which gives the ejector motive flow as a function of the inlet pressure P_{ej}, to find the motive flow $\dot{m}_1$ out of the ejector. Then Figure 13 which gives the recycle ration as a function of the motive flow was used to find the recycle ratio of the ejector at those conditions. The total flow through the stack was then calculated using (16) and (17). The pressure drop from the inlet manifold to the outlet manifold at the same current was taken from Figure 7. The resulting flow versus pressure drop for the stack was then in Figure 8.
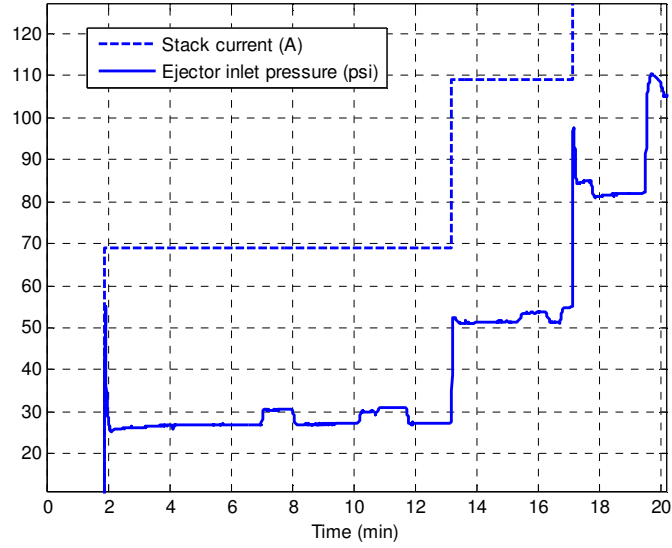
Figure 6: Anode pressure drop testing

Figure 6 shows the increase in the inlet pressure to the ejector as a larger current is drawn

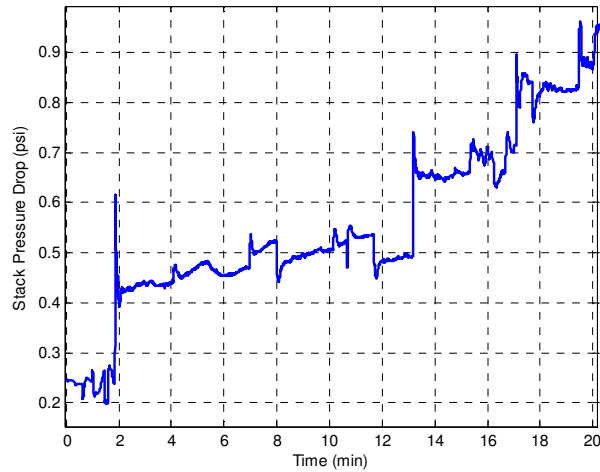from the system requiring a greater flow rate into the stack.

Figure 7: Anode outlet pressure during testing

Figure 7 shows the corresponding increase in pressure drop through the stack as the flow

rate increases. From this data we arrive at the following values for $k_{im,fc}$ and $k_{fc,om}$ by

approximating the pressure drop at each to be 50% of the total pressure drop.
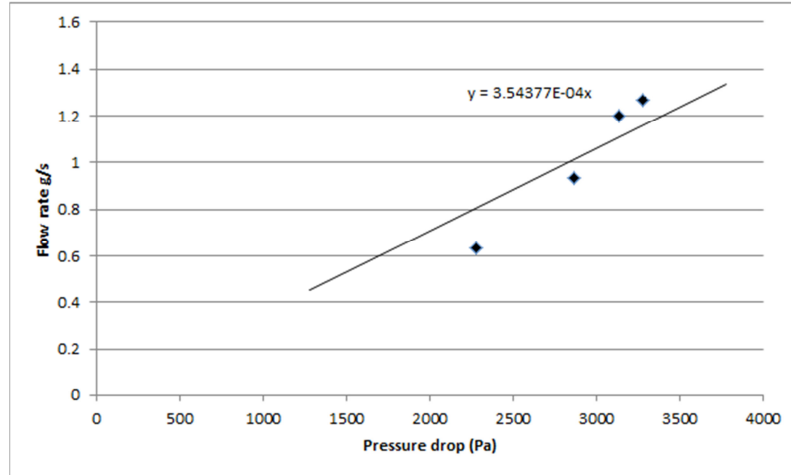
36

Figure 8: Linear nozzle constant for the stack to manifold interface

The resulting flow versus pressure drop data is plotted in Figure 8 from which $k_{im,fc}$ and

$k_{fc,om}$ are found to be

$$k_{fc,om} = k_{im,fc} = 3.5438 * 10^{-4} \frac{g/s}{Pa}$$

The stack's model parameters are summarized in Table 1.

Table 1: Stack model parameters

k_{im}	Inlet manifold dynamic constant	2.2094×10^7 Pa/g
k_{fc}	Stack dynamic constant	1.957×10^5 Pa/g
k_{om}	Outlet manifold dynamic constant	6.581×10^6 Pa/g
$k_{im,fc}$	The linear flow constant btwn the inlet manifold and the	3.5438×10^{-4} g/s/Pa
$k_{fc,om}$	The linear flow constant btwn the stack and the outlet	3.5438×10^{-4} g/s/Pa

From Table 1 it can be observed that the largest volume in the system is within the stack,

and thus its pressure dynamic will have the longest time constant in the system.

4.2 Identification of ejector model parameters

The ejector parameters were identified by using a drawing of the ejector to obtain the geometries, and by experimental results. The ejector was tested using dry hydrogen in the lab. The test schematic in Figure 9 shows the experimental set up of the ejector test stand (also shown as built in Figure 10), and Table 1 describes the instrumentation used.

Figure 9: Ejector test stand PI&D

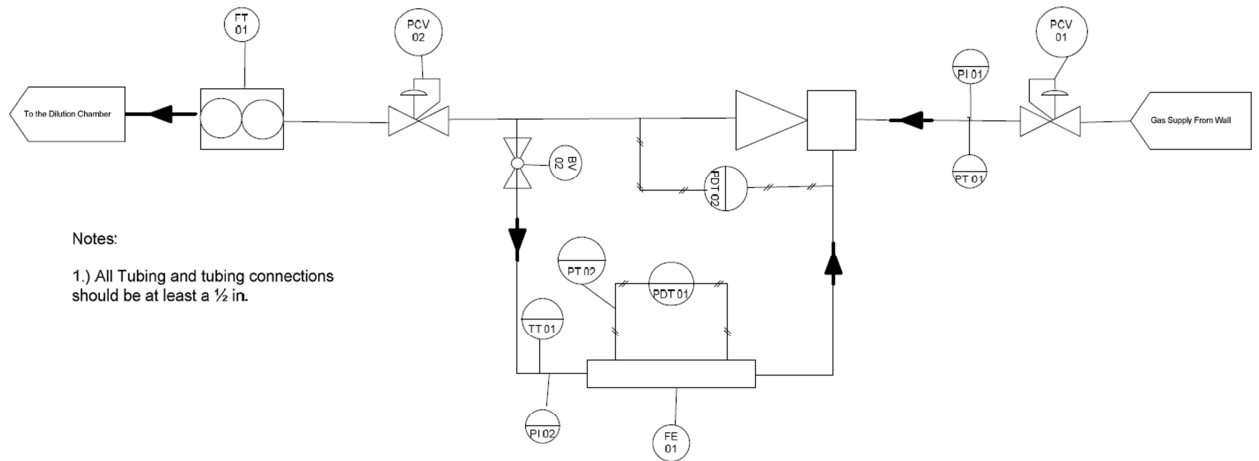The hydrogen gas is supplied from the wall and regulated to create the desired motive flow rate which is measured at FT01. The back pressure is set using the back pressure regulator PCV 02. The resulting flow is measured using the laminar flow element FE01 and the gas temperature is measured using a thermocouple denoted as TT01. The specifications accuracy of the equipment used is listed in Table 2

Table 2: Ejector test stand equipment and accuracy

| P&ID Tag	Description	Manf	Model	Other	Range	SN#	accuracy
FT01	Ejector exit flow meter	Alicat Scientific	M250SLPM-D/5M	Gas H2 TOT	0-250 SLPM	47388	0.3% reading +0.2% FS
TT01	Thermocouple	Omega	K-Type	NIST Thermocouple curve	-200 to 1250 C		1.1C
FE01	Laminar flow element	Merriam	Z50MW20-1	Series: 740590-J1 0-7.0496 CFM at 8 in H2O @ 70F and 29.92 in Hg abs	0-1000 SLPM	C740590J417	0.72% of reading
PDT01	Differential pressure transducer	Setra	239	0-10V output	0-15 in. WC	3565703	0.14% FS
PDT02	Differential pressure transducer	Setra	239	0-5V output	0-10 psid	3565799	0.14% FS
PT01	Pressure transducer	Setra	209	P/N 1200PG2M2402	0-200 psig		0.25% FS
PT02	Pressure transducer	Setra	209	P/N 1025PG2M2402	0-25 psig		0.25% FS
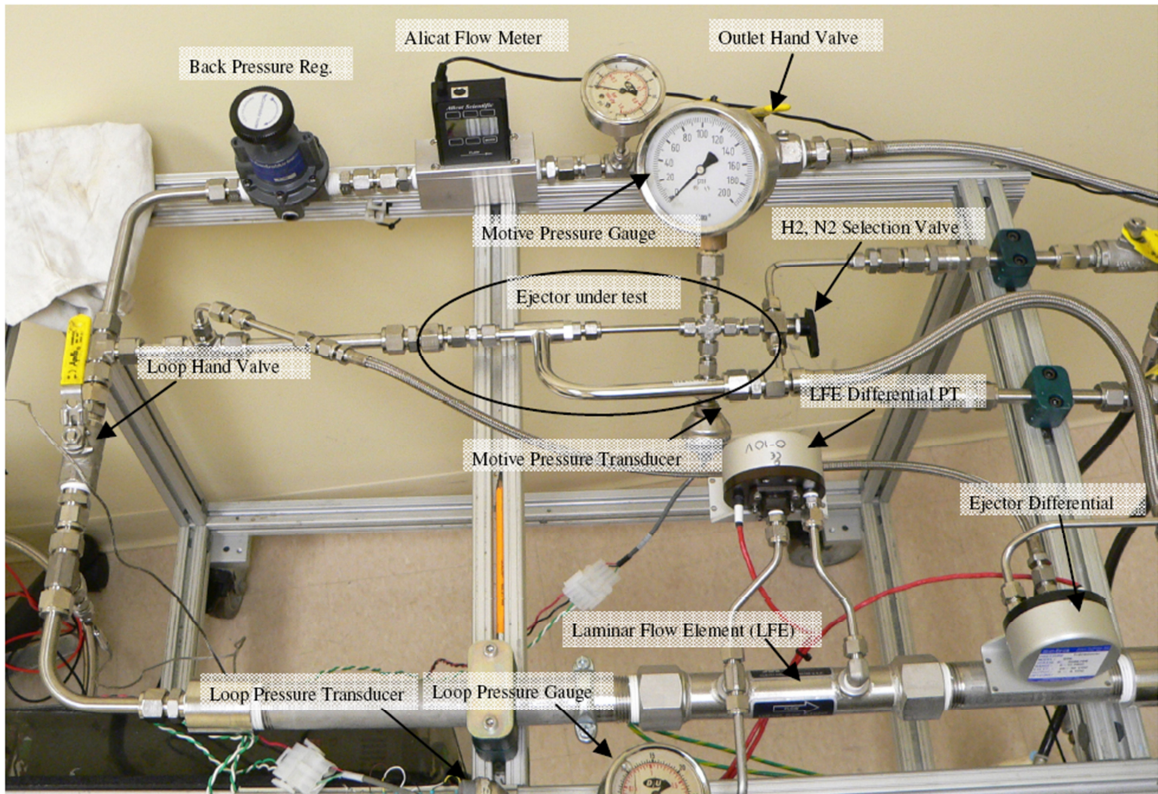
Figure 10: Ejector test stand as built

Figure 10 shows the completed test stand with additional nitrogen supply to safely purge the system of air prior to use with hydrogen. The entrainment ratio of the ejector was measured using this test stand for primary flows of 2, 4, 6, 8, 10, 12, and 14 g/min of hydrogen and at secondary flow back pressures of 7, 9 and 11 psi. The resulting entrainment ratios are shown in Figure 13: Ejector entrainment ratio from testing.

Table 3: Ejector test results

Primary mass flow rate (g/min)	Secondary flow pressure (psi)	Entrainment ratio		
		Ejector 1	Ejector 2	Ejector 3
2	7	4.04	4.10	4.25
2	9	3.77	3.78	3.91
2	11	3.49	3.53	3.63
4	7	5.19	5.19	5.28
4	9	4.67	4.67	4.82
4	11	4.37	4.34	4.46
6	7	5.68	5.33	5.29
6	9	5.35	5.00	4.95
6	11	5.02	4.73	4.62
8	7	5.57	5.22	5.23
8	9	5.35	4.90	4.96
8	11	5.01	4.67	4.72
10	7	5.35	5.25	5.10
10	9	5.04	4.99	4.86
10	11	4.82	4.77	4.65
12	7	5.05	4.99	4.89
12	9	4.82	4.75	4.68
12	11	4.65	4.58	4.51
14	7	4.83	4.78	4.68
14	9	4.60	4.54	4.46
14	11	4.45	4.38	4.34

By plotting the motive flow through the ejector versus the pressure drop through the ejector orifice as shown in Figure 11, the mass flow rate of the primary flow can be approximated linearly from the pressure drop.
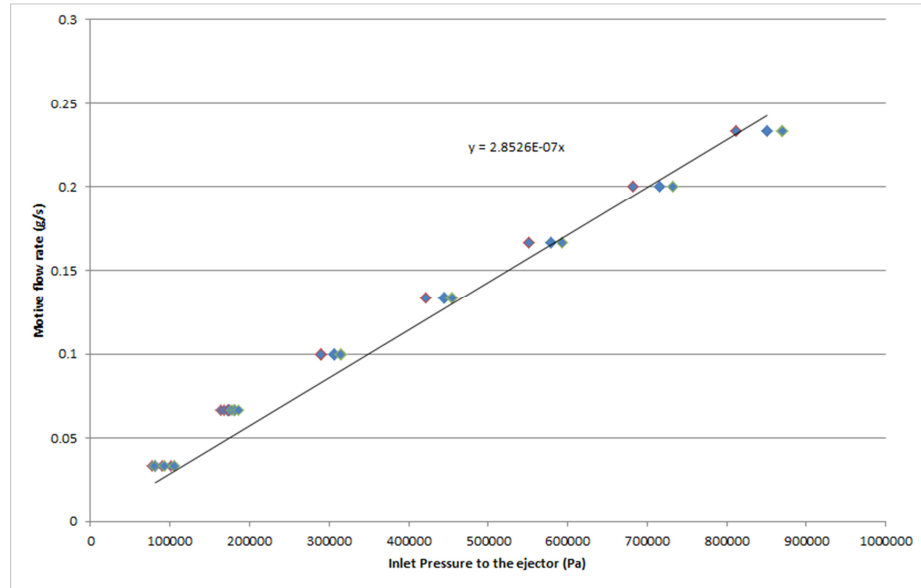

Figure 11: Ejector pressure inlet versus primary flow

Fitting a linear trend line to this data and converting the units of flow to g/s and the units of pressure to Pa. The value of k_{ej} is found to be 2.8526×10^{-7}(g/s)/Pa.
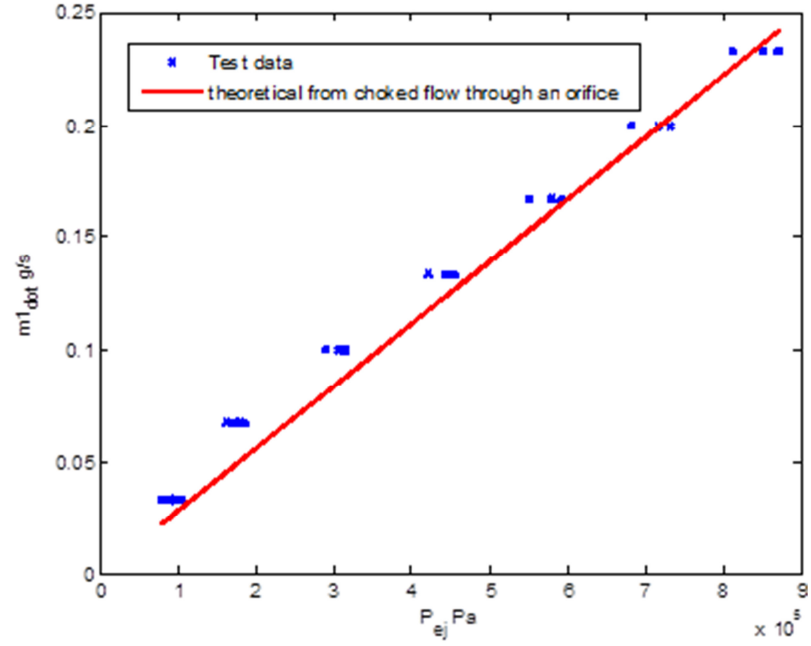
Figure 12: Ejector primary flow rate versus theoretical choked flow rate

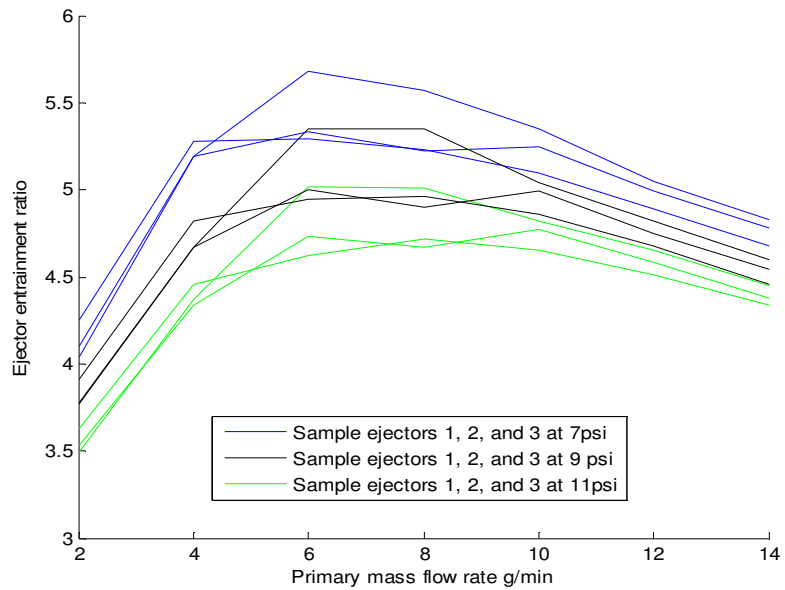The data from Table 3 is plotted in Figure 13.

Figure 13: Ejector entrainment ratio from testing

43

The ejector entrainment ratio can be approximated to be 5 over the majority of the control range, however for the nonlinear model a 3 dimensional polynomial was fitted to the data. The coefficients of the poly nominal where dependent on P_{om} the pressure in the outlet manifold. The equations used in the nonlinear model are

$$\omega(\dot{m}_1, P_{om}) = a_1(\dot{m}_1 60)^3 - a_2(\dot{m}_1 60)^2 + a_3(\dot{m}_1 60) + a_4 , \tag{85}$$

where

$$a_1 = -0.0104 P_{om} + 2251.5 , \tag{86}$$

$$a_2 = -0.0044 P_{om} + 1024.7 , \tag{87}$$

$$a_3 = -0.0004787 P_{om} + 128.66, \tag{88}$$

and

$$a_4 = -1.066 * 10^{-5} P_{om} + 4.223. \tag{89}$$

The ejector's linearized model parameters are summarized in Table 4.

Table 4: Ejector model parameters

k_{ej}	The linear flow constant for the ejector	2.8526×10^{-7} (g/s)/Pa
ω	Ejector entrainment ratio	5

4.3 Identification of the PCV model parameters

The pressure control valve has several parameters associated with it that need to be identified through mechanical measurements and experimental results. The valves performance is dependent on its spring constant K_{sp}, kinematic friction μ_k, piston mass m, piston area A_{piston}, spring initial offset x_{offset}, maximum travel of the piston x_{max}, area of the valve seat A_{seat}, and maximum flow coefficient k_{max}. The supply pressure to the control valve is delivered by an upstream regulator that controls the hydrogen pressure downstream of the supply tanks. The tanks are filled to approximately 5500 psi and drain slowly over an operating period of about 4-6 hours depending on the load profile of the application. The regulator will control the pressure to the pressure control valve to within the range of 175 to 225 psi, and can be considered constant over time scales of 10 minutes or less.

4.3.1 Identification of K_{sp}

The spring force was found by using the linear spring force equation

$$F_{spring} = K_{sp}\Delta x, \tag{90}$$

where Δx is the change in length of the spring from its free length for a given force. This was obtained by first measuring the spring's free length using a set of digital calipers with an accuracy of 0.001in. A force of 51.8175N was then applied to the spring and the spring length was measured again. The free length was measured at 0.985in and the compressed length was measured at 0.334in. The change in length was found to be 0.017m. Using 51.8179N $= k_{spring} 0.017m$, we obtain a spring constant K_{sp}=3048 N/m.

45

4.3.2 Identification of μ_k

In order to determine the frictional coefficient μ_k, three valve piston samples were tested on an Instron machine with the spring and valve body removed so that only the static and kinematic frictional forces are affecting the motion.

Figure 14: Valve piston in body

The static force of the first samples was in error due to the piston being at a slight angle inside the valve. The static force of samples 2 and 3 were averaged, and lead the static frictional force to be 17.96N.

The kinetic friction was taken to be the average of the three samples when the piston's position was greater than 2mm, and was found to be 10.61N.
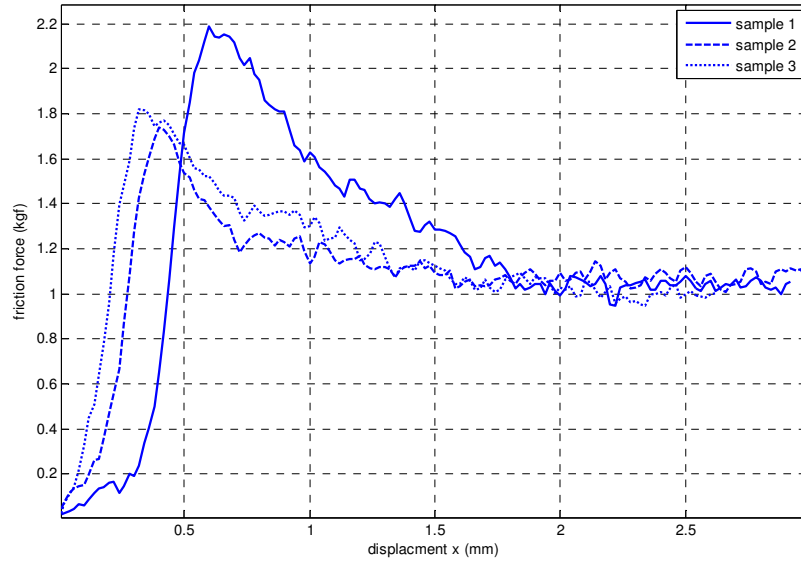
Figure 15: PCV friction measurement

The piston's velocity was a constant 1 mm/s during the test as shown in Figure 16, and

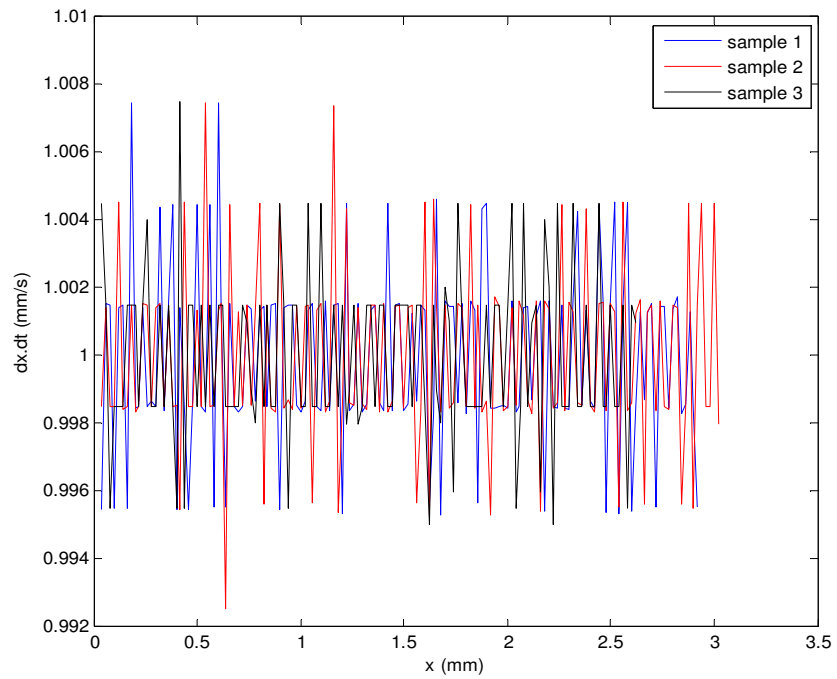the force measured is the frictional force on the plunger, giving a value of 10610 N/(m/s)

for μ_k.

Figure 16: PCV's piston velocity during friction measurement

4.3.3 Identification of K_{max}

In order to determine the maximum flow constant of the valve with hydrogen, the valve was tested in the lab using an Alicat mass flow meter and two pressure transducers in order to measure the pressure drop versus flow for the valve when it is fully open. The Alicat accuracy is 0.3% of the reading and 0.2% of full scale, and the pressure transducers used to measure the upstream and downstream pressures have an accuracy of 0.25% of full scale. The pressure drop through the valve was measured at mass flow rates between 2 and 14 g/min. The results of the testing are shown in Figure 18.
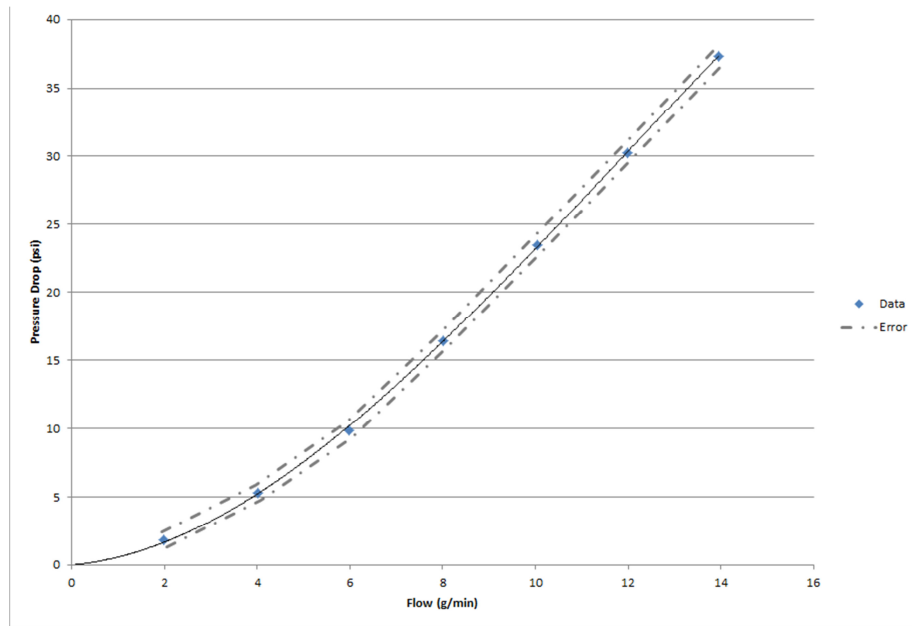

Figure 17: PCV pressure drop versus flow

The relationship shown here is nonlinear, however since we need a linear relationship for k_{max} the data is re-plotted in Figure 18 and the slope of best linear fit which passes through zero is taken for the estimation of k_{max}.
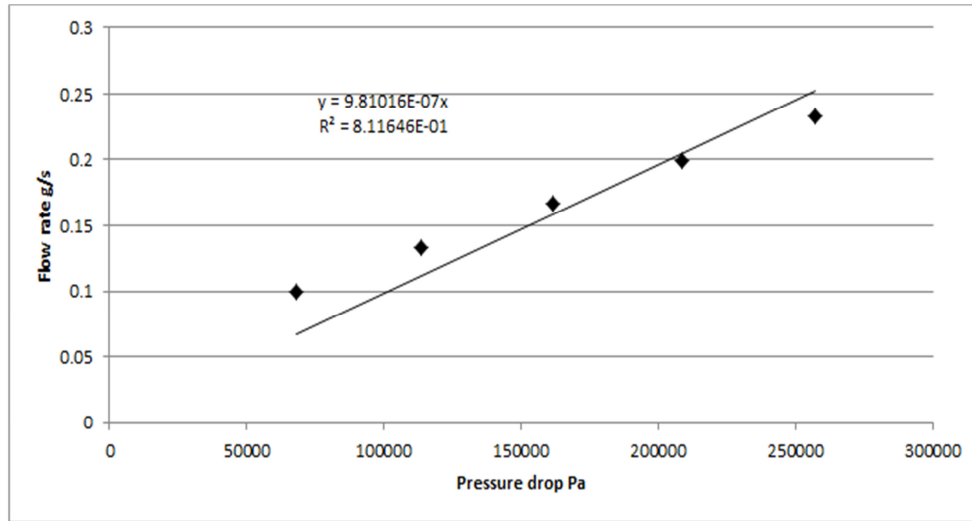
Figure 18: PCV Kmax testing

The max flow constant for the valve is $9.81*10^{-7}$ (g/s)/Pa.

4.3.4 Identification of A_{piston} and m

The piston's plunger, shown in Figure 19, was removed from the valve and its diameter was measured with a pair of digital micrometers with an accuracy of 0.001in. The diameter was measured to be 1.477 in. From the diameter measurement, the area was found to be $A_{piston} = 0.001257\text{m}^2$. The piston was then weighed on an Acculab SV30 scale, with a resolution of 0.005kg. The piston's mass was measured to be $m = 0.040kg$.
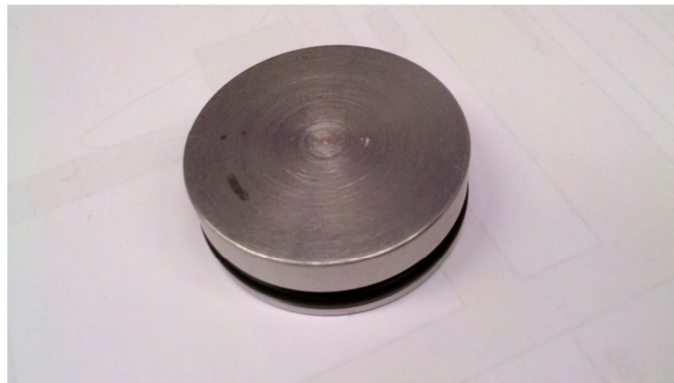

Figure 19: PCV piston

49

The parameters of the PCV's piston are thus:

$$A_{piston} = 0.001257m^2 \text{ and } m = 0.040kg.$$

4.3.5 Identification of A_{seat}

The area of the seat was found by removing the plunger from the valve and measuring the valve seat using the same pair of digital micrometers with an accuracy of 0.001in. The seat was measured to have a diameter of 0.137in. From this measurement, the area of the seat is calculated to be $A_{seat} = 9.51 * 10^{-6} \ m^2$.

4.3.6 Identification of x_{max}

The maximum travel of the piston, x_{max}, was found by measuring the change in position from the free position of the PCV piston to the fully compressed position. The change in position was measured using the micrometers with accuracy of 0.0254 mm and was found to be 0.003m.

4.3.7 Identification of x_{offset}

The initial compression of the spring when assembled in the pressure control valve was found by referring to the manufacturer's drawing of the valve, and is 0.01m.

4.3.8 Summary of the PCV's model parameters

Table 5: Summary of PCV parameters

symbol	definition	Value
A_{piston}	The area of the piston	0.001257m^2
A_{seat}	The area of the valve seat	$9.51 \text{ x} 10^{-6} \text{ m}^2$
x_{max}	The maximum travel of the piston	0.003 m
x_{offset}	The initial Δx of the spring	0.010 m
K_{sp}	The spring constant	3048 N/m
μ_k	The coefficient of kinetic friction	10610 N/(m/s)
k_{max}	The max flow constant of the valve	$6.6747 \text{x} 10^{-8}$ (g/s)/Pa
P_s	The supply pressure	$1.0341 \text{ x} 10^6$ Pa
m	The mass of the piston	0.040 kg

These values are implemented in the model to simulate the current pressure control valve design. For optimization purposes the area of the piston, the spring constant, and the mass of the plunger are considered.

Chapter 5. Simulations and PCV optimization

5. Introduction

In this chapter the parameters in Chapter 4 are applied to the models developed in Chapter 3. The closed loop model of the fuel cell and the plant is implemented in Simulink and is compared to laboratory testing of the system for validation. The output of the model created from the linearized dynamics is also compared to the nonlinear model. With knowledge of the validity of the linearized model, the eigenvalues of the closed loop state matrix of the linearized system are calculated, and their sensitivity to the PCV's parameters is analyzed.

5.1 Model implementation

The linear model of the fuel cell plant was implemented in Simulink by using a state space block and defining A, B, C, and D as described in the equation (33) for the linear plant.
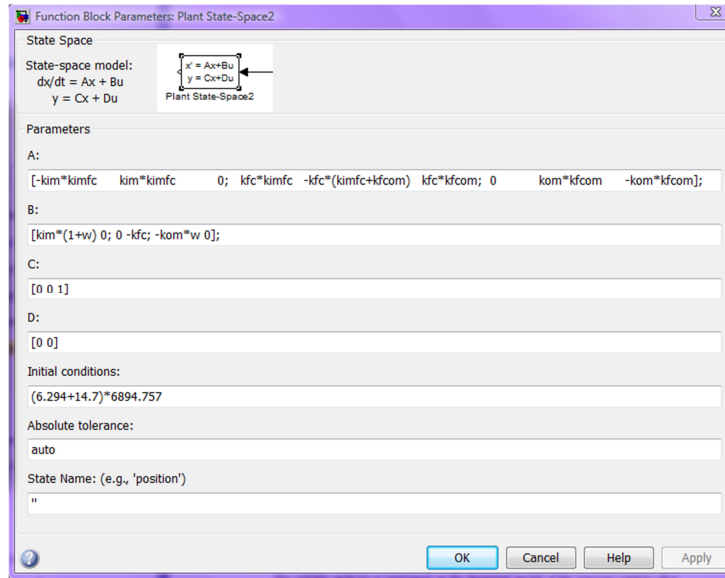
Figure 20: Linear implementation of the plant

The nonlinear model was implemented by implementing the equations (30) through (32) and using the function described in 4.2 for the ejector. The Simulink block diagram implementation of this can be seen in Figure 21. The recycle flow rate $\dot{m}_6$ is an input to this model from the ejector model whose implementation is shown in
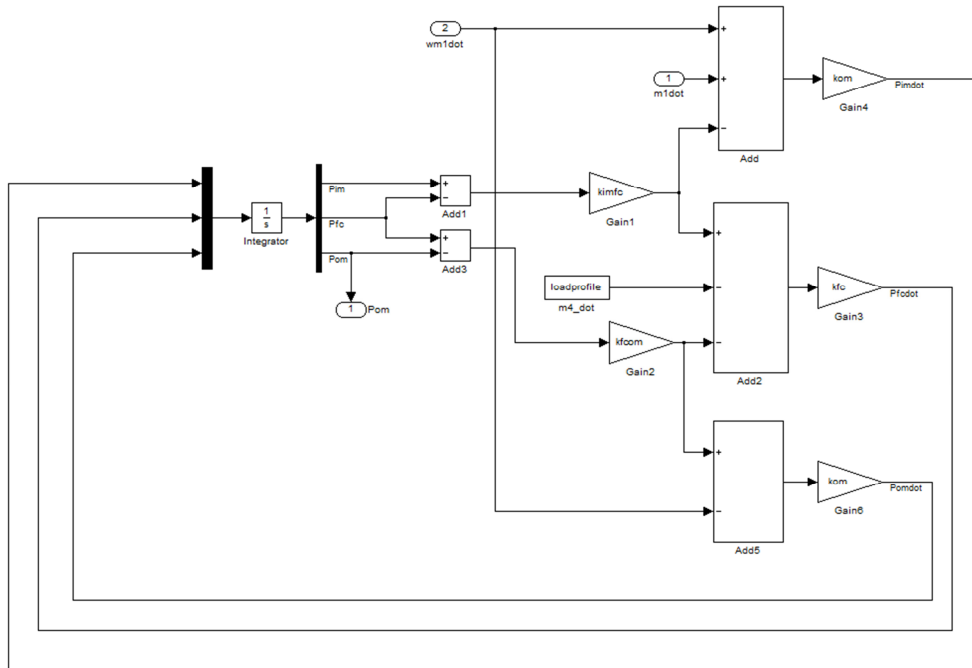
Figure 21: Nonlinear implementation of the fuel cell plant
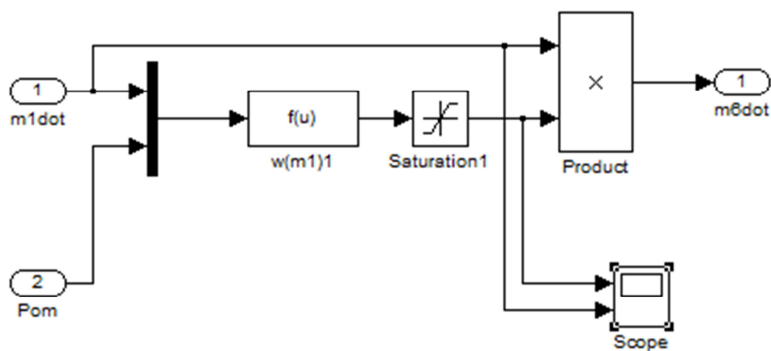

Figure 22: Ejector model

The linear model for the PCV valve was also implemented using a state space block, but with the matrices give in the linearized valve model equation (75) and (76). The nonlinear model was implemented directly from equations (57) and (61) in Simulink. The Simulink block diagram for the nonlinear model of the PCV is shown in Figure 23.
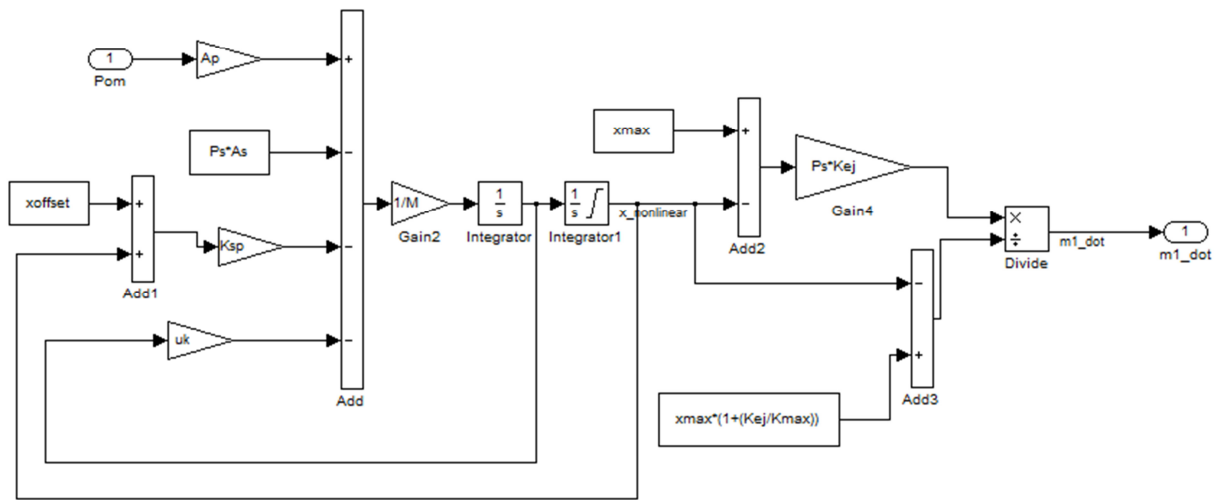
Figure 23: Nonlinear implementation of the PCV model

These three models were made into subsystems which were connected to simulate the closed loop system. The connected system is shown in Figure 24.
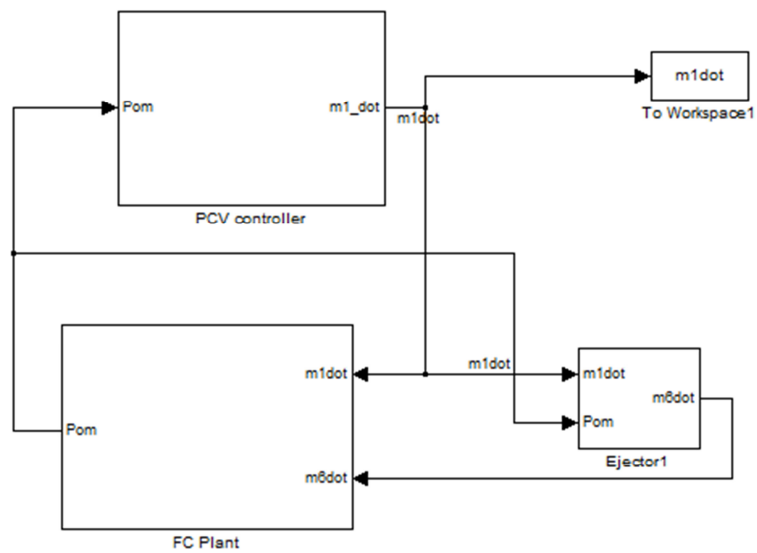

Figure 24: Nonlinear closed loop system implementation

The constants in the simulation were then initialized with the values from Chapter 4. These values are summarized in table below.

Table 6: Summary of model parameters

symbol	definition	Value
A_{piston}	The area of the piston	0.001257m^2
A_{seat}	The area of the valve seat	$9.51 \times 10^{-6} \text{ m}^2$
x_{max}	The maximum travel of the piston	0.003 m
x_{offset}	The initial Δx of the spring	0.010 m
K_{sp}	The spring constant	3048 N/m
μ_k	The coefficient of kinetic friction	10610 N/(m/s)
k_{max}	The max flow constant of the valve	6.6747×10^{-8} (g/s)/Pa
P_s	The supply pressure	1.0341×10^6 Pa
m	The mass of the piston	0.040 kg
k_{ej}	The linear flow constant for the ejector	2.8526×10^{-7} (g/s)/Pa
ω	The ejector entrainment ratio	5
k_{im}	Inlet manifold dynamic constant	2.2094×10^7 Pa/g
k_{fc}	Stack dynamic constant	1.957×10^5 Pa/g
k_{om}	Outlet manifold dynamic constant	6.581×10^6 Pa/g
$k_{im,fc}$	The linear flow constant between the inlet manifold and the stack	3.5438×10^{-4} g/s/Pa
$k_{fc,om}$	The linear flow constant between the stack and the outlet manifold	3.5438×10^{-4} g/s/Pa

5.2 Model validation

The model is validated through the comparison of the simulated pressure in the outlet manifold over the same current profile as was tested on a system in the lab. In order to test the system against the model a stack with manifolds, ejector and pressure control valve was outfitted with additional pressure sensors. The pressure was measured for comparison to the model at the inlet to the ejector, at the inlet manifold, and at the outlet manifold. The mass flow rate $\dot{m}_4$ was calculated from the current drawn from the stack during the test. Applying this demand to the nonlinear model implemented in Simulink overall showed a good match in the system dynamics as can be seen in Figure 25. The settling time of both is approximately equal and the steady state values are nearly the same. It did show however a smaller change in P_{om} than seen in the lab data. This difference in the dynamics may be caused by the purging action which occurs during lab testing. The purge is an additional intermittent mass flow rate out of the stack manifold to remove nitrogen from the system. Additionally, the dynamics may be slightly different due to the molar mass during the system test being different than the one used in the simulation, however the test infrastructure to determine if this is the case is unavailable.
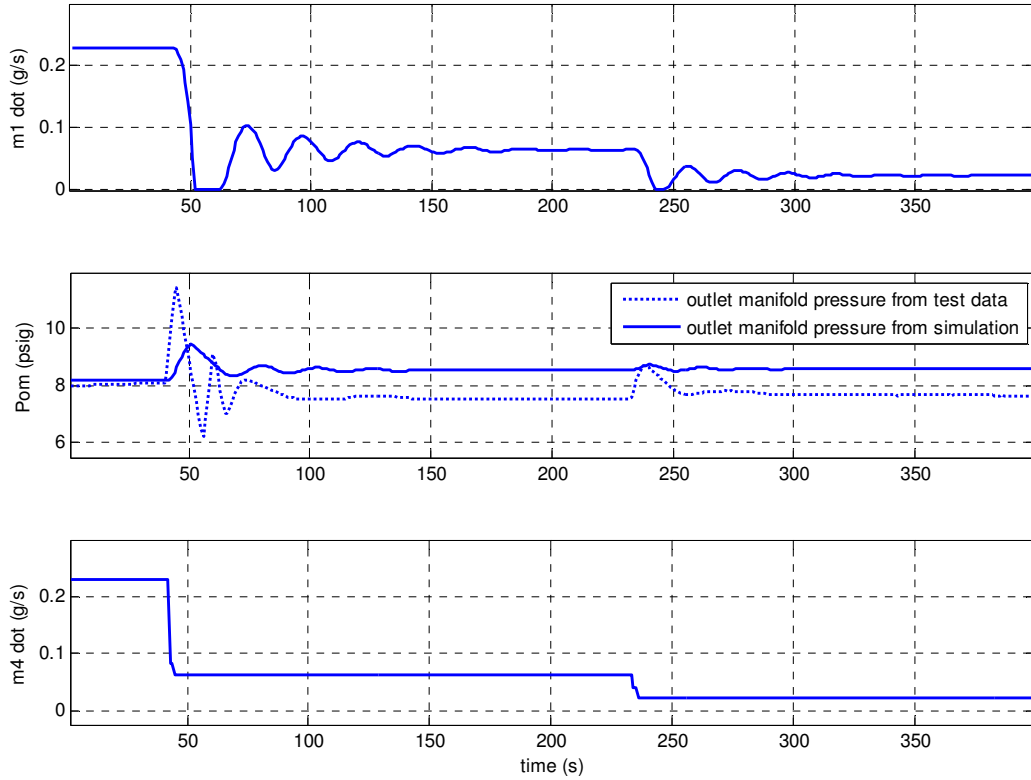
Figure 25: Simulation versus lab test results

The stability analysis is performed on the linearized model of the pressure control valve. It is therefore important to check the validity of the linear model. To do this, the linear displacement of the valve piston, x, is plotted from both the linear and nonlinear model. It can be seen in Figure 26 that the linear model slightly over predicts the displacement x of the piston at both low and high flow rates of $\dot{m}_1$. However the mid range is very accurate and based on this the linear model is considered to be a good approximation of the nonlinear dynamics and can be used to perform the stability analysis on the valve. The parameters are studied individually for their effect on the system's stability and then optimized together to obtain the most responsive and robust system.
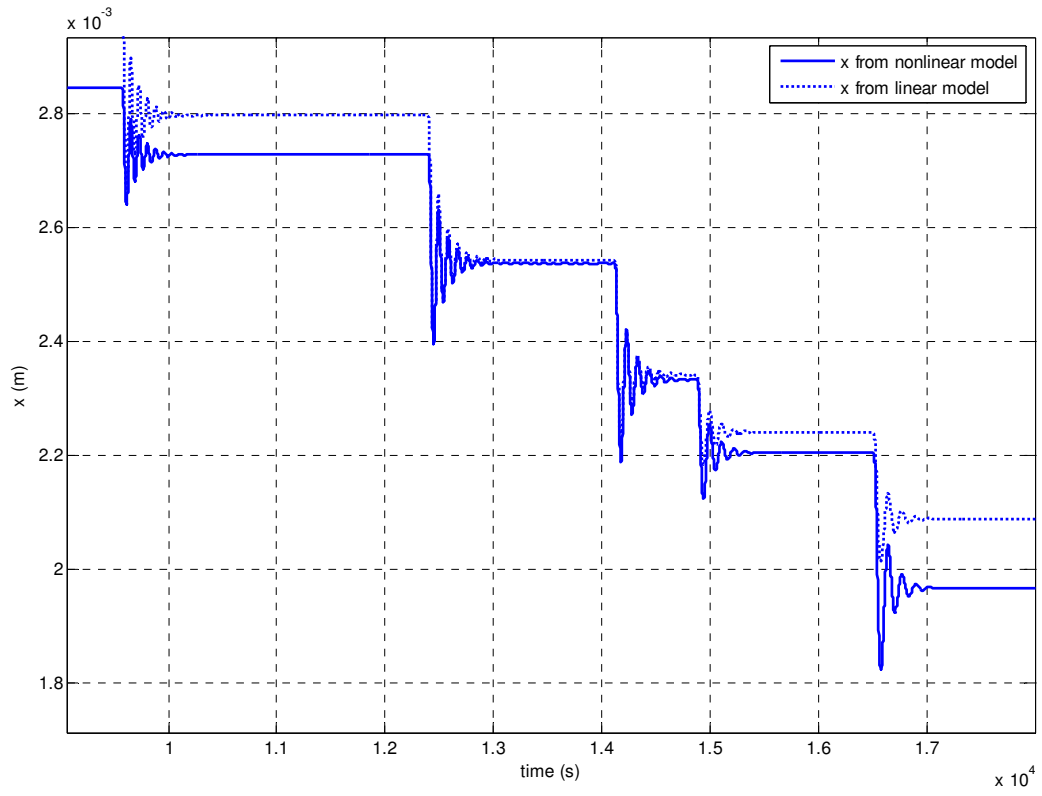
58

Figure 26: Comparison of the piston displacement x in the linear and nonlinear models

5.3 Stability of the plant

Returning once again to equation (32), now that the linearized model is validated,

the values of k_{im}, k_{fc}, k_{om}, $k_{im,fc}$, and $k_{fc,om}$ are inserted into A which results in

$$A = \begin{bmatrix} -676.2 & 676.2 & 0 \\ 14.26 & -51.9 & 14.26 \\ 0 & 150.2 & -150.2 \end{bmatrix}. \tag{91}$$

By determining the eigenvalues of A, it can be shown that the system has two

negative poles on the real axis at -690.9 and – 164.1 and one pole at zero as identified in
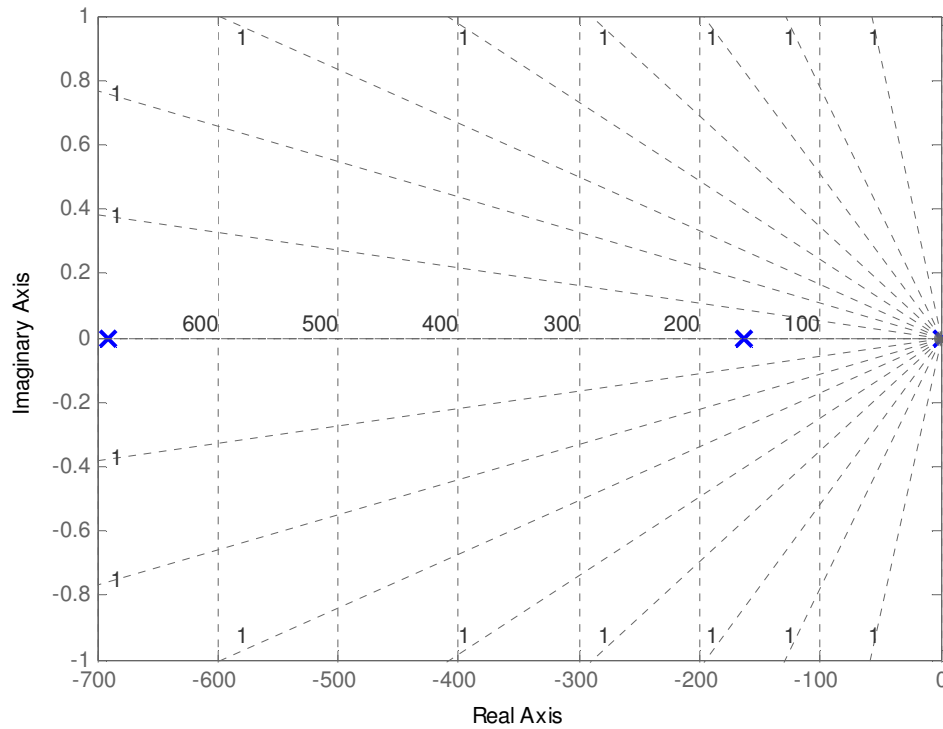
Chapter 3, and shown in Figure 27.

Figure 27: Poles plot for the fuel cell plant

5.4 Stability of the controller

Using equation (77) and inserting the values from the PCV testing we have:

$$\begin{bmatrix} \dot{x}_1 \\ \dot{x}_2 \end{bmatrix} = \begin{bmatrix} 0 & 1 \\ -76200 & -265250 \end{bmatrix} \begin{bmatrix} x_1 \\ x_2 \end{bmatrix} + \begin{bmatrix} 0 \\ -4.996 \end{bmatrix} P_{om}, \tag{92}$$

the poles of which are both negative, as shown in Chapter 3 and are at -265249.7 and -0.2837.

5.5 Stability and performance of the plant and controller

The stability of the system with the plant and the controller can be analyzed by looking at the eigenvalues of the closed loop system's state matrix in (84). By using the values of the parameters identified in chapter 4, the state matrix is

$$H = \begin{bmatrix} -676.2 & 676.2 & 0 & 11436000 & 0 \\ 14.26 & -28.52 & 14.26 & 0 & 0 \\ 0 & 150.2 & -150.2 & -2116500 & 0 \\ 0 & 0 & 0 & 0 & 1 \\ 0 & 0 & 4.996 & -76200 & -265250 \end{bmatrix}.$$

The eigenvalues of H are λ_1= -265249.7, λ_2= -690.9, λ_3= -164.3, λ_4= -0.01712 + 0.8228i and

λ_5= -0.01712 - 0.8228i.

Eigenvalues λ_2 through λ_5 can be seen in Figure 28. λ_4 and λ_5 have a small negative real parts and an imaginary part, which results in the long settling time and the oscillatory behavior noticed in Figure 25. By adjusting the parameters of the valve, eigenvalues that are more negative and real can be produced, thus reducing the response time and oscillation of the system.
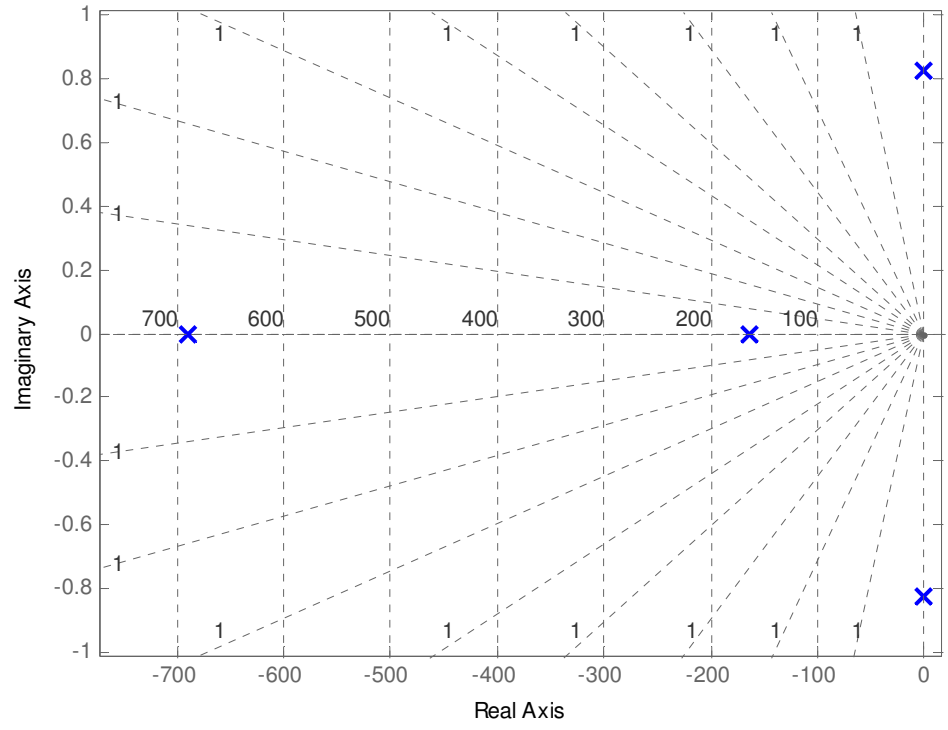
Figure 28: Nominal closed loop system poles

5.6 Closed system parameter optimization

Beginning this analysis with K_{sp}, it can be seen in Figure 29 that the eigenvalues of H decrease as K_{sp} increases. A 10% change in K_{sp} results in a 83.7% decrease in the real part of the eigenvalues of H. If the stiffness of the spring is increased the system will require a greater change in pressure for the same change in x, or rather will have a more controlled response, preventing the oscillations see in Figure 25, however there is a practical limit of the change in K_{sp} because it is desirable to keep the pressure in the outlet manifold from exceeding 10 psig. This limit is at 1.1154×10^8 N/m, with no other changes to the parameters based on (62) presented in section 3.4.
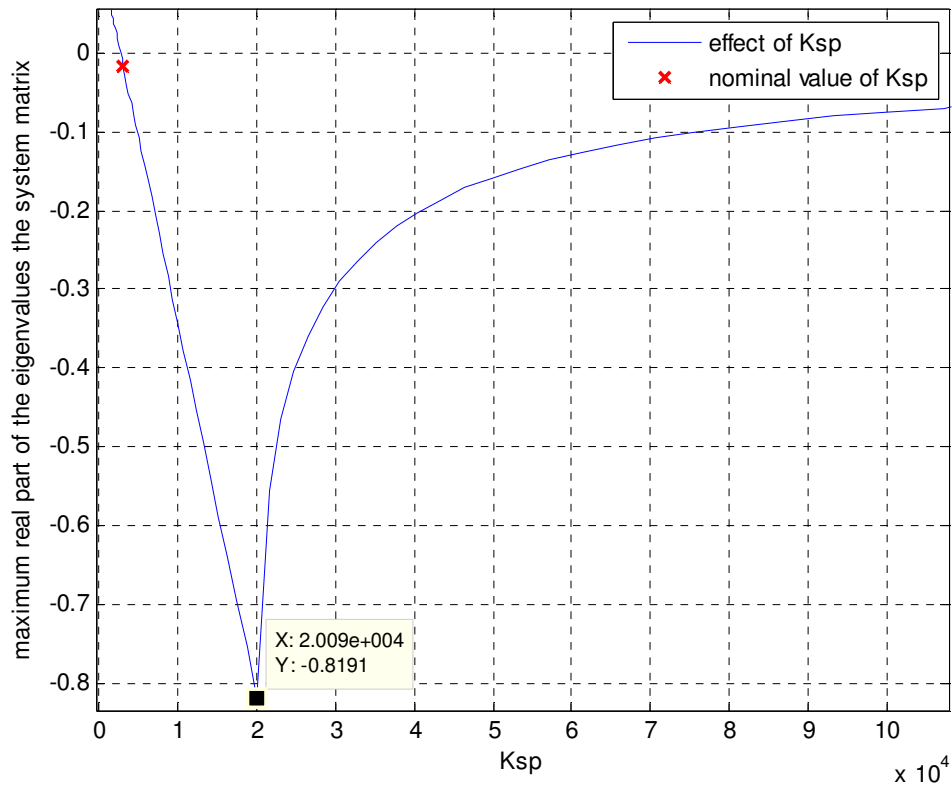

Figure 29: Effect of K_{sp} on the closed loop system's performance

Figure 30 shows the results of performing the same sensitivity study of the maximum real part of the eigenvalues of the system to changes in the area of the piston A_{piston}. The system's performance increases as the area of the piston is decreased. A 10% change in A_{piston} results in a 73.7% change in the maximum real part of the eigenvalues of the system matrix. The system performance improves as the piston area becomes smaller, once again this would cause the pressure in the outlet manifold to be higher prior to the response in the valve, however the piston area also has a minimum limit, which is $7x10^{-4}$ m^2 in order to maintain less than 10 psig in the outlet manifold.
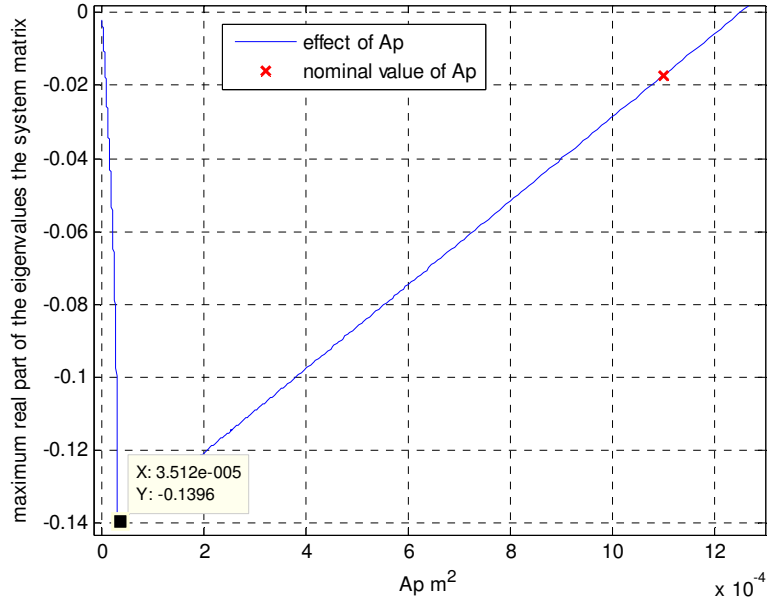

Figure 30: Effect of A_{piston} on the closed loop system's performance

Carrying out the same analysis for the piston mass, m shows that it has little to no effect on the system's performance as can be seen in Figure 31. The mass is therefore not given further consideration in this sensitivity study.
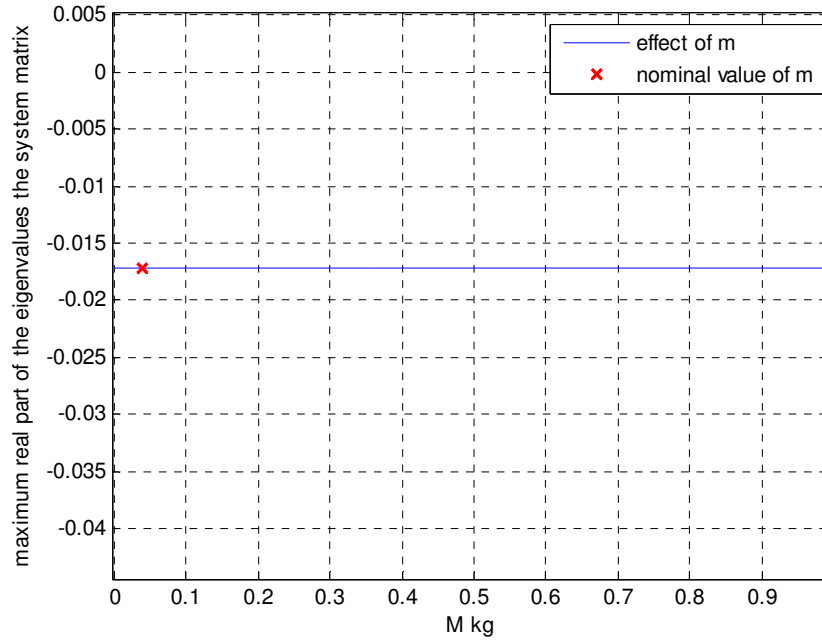
Figure 31: Effect of m on the closed loop system's performance

The coefficient of kinetic friction μ_k does have an effect on the performance of

the closed loop system as can be seen in Figure 32. Decreasing the kinetic friction

coefficient by 10% results in a 11.1% decrease in the maximum real part of the

eigenvalues of the closed loop system's state matrix. Additionally from (62) the kinetic

friction does not have an effect on the steady state value of P_{om}, however material

properties and the requirement that the valve piston seals against hydrogen limits how

much this parameter can be decreased and its optimization has less effect on the valve

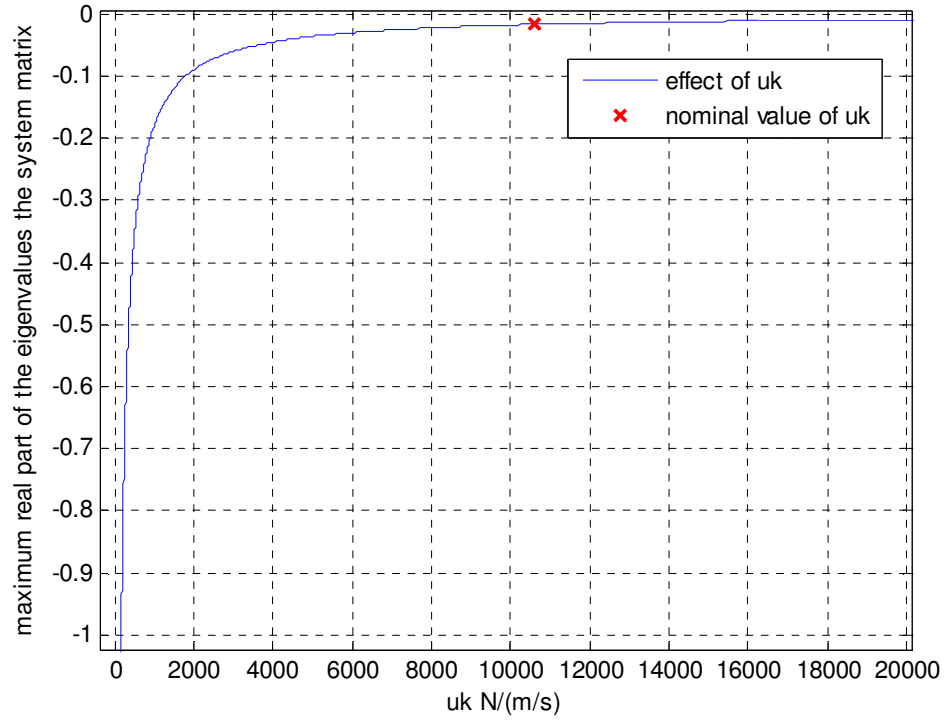performance than does the valve piston area and spring constant.

Figure 32: Stability effect of μ_k

Based on the initial sensitivity study of the valve parameters on performance and the practicality of changing them the valve is optimized around the parameters K_{sp} and A_{piston}. The solution space is shown in Figure 33.
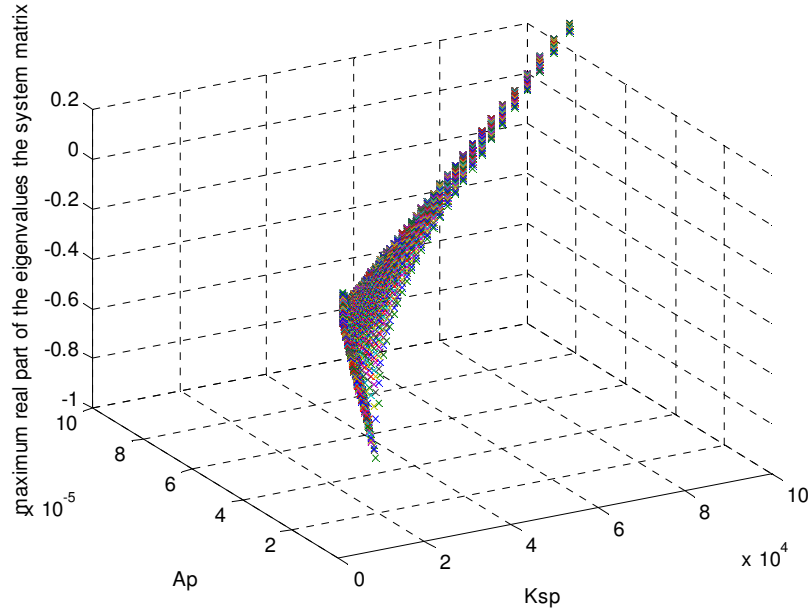
Figure 33: The solution space of Ksp and Ap

The function fmincon in MATLAB is used to determine the optimal values for the parameters K_{sp} and A_{piston} to minimize the closed loop eigenvalues. The parameter x_{offset} is also adjusted to minimize these values further without exceeding 10 psig in the outlet manifold. The resulting parameters are summarized in Table 7. The function to be minimized is the maximum of the real part of the eigenvalues of H. The constraints for this minimization are to have P_{om_max} less than 10psig, P_{om_min} greater than 5 psig, and the imaginary parts of the eigenvalues of H to be equal to zero. The code can be found in the appendix.

Table 7: Optimized PCV parameters

x_{offset}	The initial Δx of the spring	0.01236 m
K_{sp}	The spring constant	53655 N/m
A_{piston}	The piston area	0.00567 m²

67

The optimized parameters result in the following eigenvalues for the closed loop state matrix: $\lambda_1 = -2.6524*10^5$, $\lambda_2 = -690.9$, $\lambda_3 = -165.4$, $\lambda_4 = -1.86$ and $\lambda_5 = -1.86$.

Placing the optimized values into the simulation and comparing to the nominal parameters shows a significant improvement in the system's operation as can be seen in Figure 34. The figure shows a faster settling time and a more damped behavior of $\dot{m}_1$ and P_{om}.
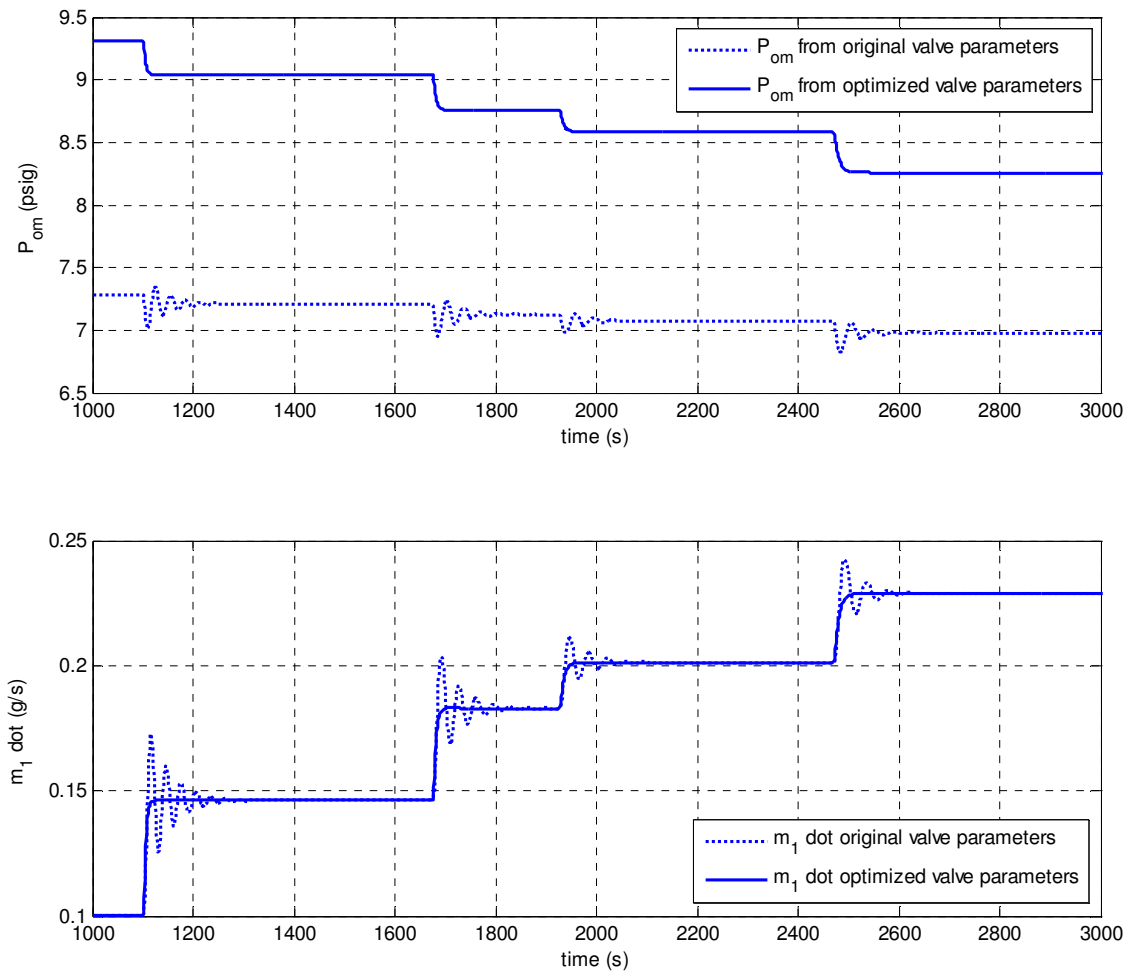

Figure 34: Simulated performance improvement

Chapter 6: Conclusions

The relevant dynamics of the fuel cell, manifolds, ejector, and pressure control valve are modeled through first principles. The model which results is nonlinear. For the purposed of stability analysis the model is linearized. The parameters necessary to implement the model are gathered through lab testing and analysis. The parameters are linearized where applicable for implementation in the linear model. Both the linear and nonlinear models are implemented in Simulink and tested against lab data take from the system being modeled. Though the data did not match the output of the system exactly, the results showed the same time constant and dynamic behavior as the system. Since the model did capture the systems dynamic response the linearized model of the valve is used to perform the optimization of the valve parameters. The optimized parameters are then implemented into the nonlinear model of the system and the results are compared to the original parameters.

The improved parameters show a significant improvement in the systems response to step changes in current. The improved parameters result in a faster response of the system to step changes in current and also eliminated the oscillations seen in the original model. What is found is that the system's performance can be improved by increasing the stiffness of the spring which is used in the pressure control valve. However, the system is constrained by the requirement to keep the pressure in the outlet manifold below 10 psig for optimal ejector performance, since its entrainment ratio decreases at higher back pressures, and also to ensure a low rate of gas cross over due to a high partial pressure differential between the anode and the cathode in the stack. In

69

order to maintain the current system performance with the ejector and optimize the valve

the initial offset of the valve is used to adjust the system pressure P_{om} at the optimized

values. The area of the piston is increased with the result that the same pressure in the

outlet manifold as had previously would result in a larger force from the piston on the

spring in the optimized valve. In this way the ejector performance is not compromised by

a higher back pressure at the anode inlet. The lower pressure also ensures that the system

is not susceptible to additional gas cross over. The system could be further optimized by

reducing the kinetic friction μ_k, however the feasibility of improving the friction

coefficient would require a study of hydrogen compatible seals and their frictional

properties. In conclusion the system, with the current frictional coefficient, can be greatly

improved through increasing the stiffness of the spring, the area of the piston and

balancing the change by altering the initial compression of the spring.

Appendix:

A.1 Optimization code

A.1.1 optimize_valve.m

```
clear all;

%initialize all model parameters at their nominal values
global kim kfc kom kimfc kfcom xmax Kmax Kej Ps As M uk w;
kim=1.906e6;
kfc=4.0191e4;
kom=4.233e5;
kimfc=3.548e-4;
kfcom=3.548e-4;
xoffset=0.01;
Kmax=9.81e-7;
Kej=2.8526e-7;
Ps=(200+14.7)*6894.757;
As=8.6429e-5;
Ap=0.0011;
M=0.04;
uk=10610;
w=5;
Ksp=3048;
xmax=.003;

%calculate necessary values for A
alpha=(xmax*Kej)/Kmax;
beta=Ps*Kej;
l=(Kmax*Kej*Ps)/(2*(Kmax+Kej));
gam=-(alpha*beta)/(beta-l)^2;
delta=xmax-(alpha*l)/(beta-l)+(alpha*beta*l)/(beta-l)^2;

%find optimized values without constraint on zero imaginary part of
eig(H)
 v0=[Ksp*1e-3 Ap*1e3 xoffset*1e3];
options=optimset('fmincon');
options=optimset(options, 'Display','iter','MaxFunEvals', 8000, 'TolX',
1e-6, 'TolFun', 1e-6, 'TolCon', 1e-6, 'Algorithm', 'interior-point');
[v, fval] = fmincon(@maxeigofA,v0,[],[],[],[],[],[] ,@nonlinearcstr,
options)
Ksp=v(1)*1e3;
Ap=v(2)*1e-3;
xoffset=v(3)*1e-3;
%find optimized values with constraint on zero imaginary part of eig(H)
v0=[Ksp*1e-3 Ap*1e3 xoffset*1e3];
[v, fval] = fmincon(@maxeigofA,v0,[],[],[],[],[],[] ,@nonlinearcstr2,
options)

 %report optimized values
```

```
 Ksp=v(1)*1e3
 Ap=v(2)*1e-3
 xoffset=v(3)*1e-3
```

```
%report Pom max from optimized values
Pa_to_psi=0.00014503773801;
POMmaxSS=(((Ksp*(xoffset+xmax)+Ps*As)/Ap)*Pa_to_psi)-14.7
```

A.1.2 maxeigofA.m

```
function e=maxeigofA(v)

 global kim kfc kom kimfc kfcom xmax Kmax Kej Ps As M uk w; %brings in
global variables

%sets Ksp and Ap from v
 Ksp=v(1)*1e3;
 Ap=v(2)*1e-3;

%recalculates necessary values for A
alpha=(xmax*Kej)/Kmax;
beta=Ps*Kej;
l=(Kmax*Kej*Ps)/(2*(Kmax+Kej));
gam=-(alpha*beta)/(beta-l)^2;

 A=[-kim*kimfc       kim*kimfc             0          kim*(1+w)      0;
    kfc*kimfc    -kfc*(kimfc+kfcom) kfc*kfcom        0             0;
      0             kom*kfcom      -kom*kfcom     -kom*w           0;
      0                 0               0            0            1;
      0                 0          Ap/(M*gam)      -Ksp/M      -uk/M];

   e=max(real(eig(A)));

 %solves for the maximum real part of the eigen values of A and reports
the
 %value to fmincon function
```

A.1.3 nonlinearcstr.m

```
function [c,ceq]=nonlinearcstr(v)
%brings in global variables
global kim kfc kom kimfc kfcom xmax Kmax Kej Ps As  M uk w;

 %sets paramters to values from v
Ksp=v(1)*1e3;
Ap=v(2)*1e-3;
xoffset=v(3)*1e-3;

 %provides nonlinear constraint conditions, fmincon must solve for Ksp
 %Ap and xoffset such that c(1) and c(2) are both negative.
c(1)=((5+14.7)*6894.757)-(Ksp*xoffset+Ps*As)/Ap;
```

```
c(2)=((Ksp*(xoffset+xmax)+Ps*As)/Ap)-((10+14.7)*6894.757);

ceq=0;
```

A.1.4 nonlinearcstr2.m

```matlab
function [c,ceq]=nonlinearcstr(v)

global kim kfc kom kimfc kfcom xmax Kmax Kej Ps As  M uk w;


Ksp=v(1)*1e3;
Ap=v(2)*1e-3;
xoffset=v(3)*1e-3;

alpha=(xmax*Kej)/Kmax;
beta=Ps*Kej;
l=(Kmax*Kej*Ps)/(2*(Kmax+Kej));
gam=-(alpha*beta)/(beta-l)^2;
%provides nonlinear constraint conditions, fmincon must solve for Ksp
 %Ap and xoffset such that c(1) and c(2) are both negative.
%and there are no imaginary parts of the eigen values of A.

 A=[-kim*kimfc        kim*kimfc           0          kim*(1+w)      0;
    kfc*kimfc    -kfc*(kimfc+kfcom) kfc*kfcom          0           0;
       0             kom*kfcom       -kom*kfcom      -kom*w        0;
       0                0                0             0           1;
       0                0            Ap/(M*gam)      -Ksp/M     -uk/M];

ceq=imag(min(eig(A)));

c(1)=((5+14.7)*6894.757)-(Ksp*xoffset+Ps*As)/Ap;
c(2)=((Ksp*(xoffset+xmax)+Ps*As)/Ap)-((10+14.7)*6894.757);
```

References

[1] Stefano Pogutz, Angeloantonio Russo and Paolo Migliavacca, Innovation, Markets and Sustainable Energy: The Challenge of Hydrogen and Fuel Cells, Edward Elgar Publishing Limited, Cheltenham, UK. 2009

[2] N. Yousif-Steiner, Ph. Mocoteguy, D. Candusso, D. Hissel. "A review on polymer electrolyte membrane fuel cell catalyst degradation and starvation issues: Causes, consequences and diagnostic for mitigation. *Journal of Power Sources* 2009;194:130-145.

[3] Judith O'Rourke, Manikandan Ramani, Murat Arcak. In situ detection of anode flooding of a PEM fuel cell. *International Journal of Hydrogen Energy* 2009;34:6765-6770.

[4] Bao Cheng, Ouyang Minggao, Y Baolian. Modeling and control of air stream and hydrogen flow with recirculation in a PEM fuel cell system – I. control-oriented modeling. *International Journal of Hydrogen Energy* 2006;31:1879-1896.

[5] Jay T. Pukrushpan, Huei Peng, Anna G. Stefanopoulou, Modeling and control for PEM fuel cell stack system. *The Proceedings of the America Control Conference* Anchorage, AK. May 8-10, 2002.

[6] Jay T. Pukrushpan, Huei Peng, Anna G. Stefanopoulou. Control-Oriented Modeling and Analysis for Automotive Fuel Cell Systems.*Transactions of the ASME* March, 2004. Vol 126.

[7] Robert H. Perry, Don W Green. Perry's Chemical Engineers' Handbook . 7th edition. McGraw-Hill1997:10-56-10-58.

[8] B. J. Huang, J.M. Chang, C.P. Want, V.A. Petrenko. A 1-D analysis of ejector performance. *International Journal of Refrigeration*, 1999;22;354-364.

[9] Yinhai Zhu, Wenjian Cai, Changyun Wen, Yanzhong Li. Simplified ejector model for control and optimization. *Energy Conversion and management,* 2008;49;1424-1432.

[10] Yinhai Zhu, Wenjian Cai, Changyun Wen, Yanzhong Li. Fuel ejector design and simulation model for anodic recirculation SOFC system. *Journal of Power Sources,* August, 2007.

[11] Richard C. Dorf, Robert H. Bishop, Modern Control Systems 7th edition, Pearson education, Inc, Upper Saddle River, NJ, 2008.

[12] Bharat Bhushan, Modern Tribology Handbook Volume 1. CRC press, 2001 Boca Raton, FL, pp. 230-232.